

# ViCTORIA project: The LOFAR-view of environmental effects in Virgo Cluster star-forming galaxies

H. W. Edler<sup>1</sup>, I. D. Roberts<sup>2</sup>, A. Boselli<sup>3,4</sup>, F. de Gasperin<sup>1,5</sup>, V. Heesen<sup>1</sup>, M. Brüggen<sup>1</sup>, A. Ignesti<sup>6</sup>, and L. Gajović<sup>1</sup>

<sup>1</sup> Hamburger Sternwarte, University of Hamburg, Gojenbergsweg 112, D-21029, Hamburg, Germany  
e-mail: henrik.edler@hs.uni-hamburg.de

<sup>2</sup> Leiden Observatory, Leiden University, PO Box 9513, 2300 RA Leiden, The Netherlands

<sup>3</sup> Aix Marseille Univ, CNRS, CNES, LAM, Marseille, France

<sup>4</sup> INAF - Osservatorio Astronomico di Cagliari, via della Scienza 5, 09047 Selargius, Italy

<sup>5</sup> INAF - Istituto di Radioastronomia, via P. Gobetti 101, Bologna, Italy

<sup>6</sup> INAF - Astronomical Observatory of Padova, vicolo dell'Osservatorio 5, 35122 Padova, Italy

Received October XX, 2023; accepted XXXXXXXX XX, XXXX

## ABSTRACT

*Context.* Environmental effects such as ram-pressure stripping (RPS) shape the evolution of galaxies in dense regions.

*Aims.* We use the nearby Virgo cluster as a laboratory to study environmental effects on the non-thermal components of star-forming galaxies.

*Methods.* We constructed a sample of 17 RPS galaxies in the Virgo cluster and a statistical control sample of 119 nearby galaxies from the Herschel Reference Survey. All objects in these samples are detected in LOFAR 144 MHz observations and come with H $\alpha$  and/or far-UV star formation rate (SFR) estimates.

*Results.* We derived the radio-SFR relations, confirming a clearly super-linear slope of  $\approx 1.4$ . We found that Virgo cluster RPS galaxies have radio luminosities that are a factor of 2-3 larger than galaxies in our control sample. We also investigated the total mass-spectral index relation, where we found a relation for the Virgo cluster RPS galaxies that is shifted to steeper spectral index values by  $0.17 \pm 0.06$ . Analyzing the spatially resolved ratio between the observed and the expected radio emission based on the hybrid near-UV + 100  $\mu\text{m}$  SFR surface density, we generally observe excess radio emission all across the disk with the exception of a few leading-edge radio-deficient regions.

*Conclusions.* The radio excess and the spectral steepening for the RPS sample could be explained by an increased magnetic field strength if the disk-wide radio enhancement is due to projection effects. For the galaxies that show the strongest radio excesses (NGC 4330, NGC 4396, NGC 4522), a rapid decline of the SFR ( $t_{\text{quench}} \leq 100$  Myr) could be an alternative explanation. We disfavor shock acceleration of electrons as cause for the radio excess since it cannot easily explain the spectral steepening and radio morphology.

**Key words.** galaxies: clusters: individual: Virgo Cluster – radio continuum: general – galaxies: interactions – stars: formation

## 1. Introduction

Galaxies that inhabit dense environments such as galaxy clusters show a lower cold gas content (e.g. [Catinella et al. 2013](#); [Boselli et al. 2014b](#)) and a reduced star-forming (SF) activity (e.g. [Kennicutt 1983](#); [Boselli et al. 2014](#); [Boselli et al. 2016](#)) compared to those located in poorer environments. It is thought that those differences are caused by environmental processes, i.e. perturbations due to interactions with other galaxies or the intra-cluster medium (ICM). The process which is often thought to be the dominant perturbation affecting galaxies in massive ( $>10^{14} M_{\odot}$ ), low-redshift clusters is ram-pressure stripping (RPS; see [Cortese et al. 2021](#); [Boselli et al. 2022](#), for recent reviews). RPS is the removal of the interstellar medium (ISM) of a galaxy moving at high velocity  $v$  relative to the ICM. The ram-pressure scales as  $P \propto \rho v^2$  where  $\rho$  is the ICM density. Consequently, it is most effective in massive clusters where the galaxy velocities and the ICM densities are high.

RPS impacts the diffuse atomic phase of the ISM due to the advection of the loosely bound neutral hydrogen (H I) which can give rise to tails that can be traced by 21 cm line observations (e.g. [Chung et al. 2007](#)). This can also explain the truncated ra-

dial H I-profiles (e.g. [Chung et al. 2009](#)) and the statistical H I-deficiency (e.g. [Boselli & Gavazzi 2006](#)) of galaxies in clusters. Subsequent ionization of the stripped H I due to interactions with the ICM creates tails of ionized gas that are most commonly observed in the H $\alpha$  line (e.g. [Gavazzi et al. 2001](#); [Yagi et al. 2010](#); [Boselli et al. 2016](#)); as those recently observed during the GAs Stripping Phenomena in galaxies with MUSE (GASP; [Poggianti et al. 2017](#)) program and the Virgo Environmental Survey Tracing Ionised Gas Emission (VESTIGE; [Boselli et al. 2018b](#)). In some cases, RPS may also affect the dense molecular gas, which is fueling star formation, either indirectly by displacing the atomic gas or directly by displacing the molecular gas from the stellar disk (e.g. [Cramer et al. 2020](#); [Watts et al. 2023](#)); this will in turn reduce the star formation rate (SFR). The time-scale on which the star formation is quenched may depend on a number of parameters such as galaxy mass, orientation and velocity with respect to the ICM as well as the ICM density and dynamical state. Observational evidence points to quenching times of  $\leq 1$  Gyr (e.g. [Boselli et al. 2006, 2016](#); [Ciesla et al. 2016](#); [Fossati et al. 2018](#)).

Current RPS events in star-forming galaxies show tails in the atomic or ionized hydrogen distribution, as well as in the

radio continuum (e.g. Gavazzi 1978; Gavazzi et al. 1995). The radio continuum emission of star-forming galaxies is caused by cosmic-ray electrons (CRE) that were shock-accelerated in supernovae gyrating in weak magnetic fields (i.e. synchrotron radiation). Thus, it is a tracer of the SFR (Condon 1992; Gürkan et al. 2018; Heesen et al. 2019; Heesen et al. 2022). The CRE are transported by diffusion processes in the galactic magnetic fields, but may also be subject to advection through ram pressure, creating asymmetric or tailed radio continuum profiles. The advance of sensitive radio surveys, such as those undertaken with the LOw-Frequency ARray (LOFAR; van Haarlem et al. 2013), allowed the identification of >100 ongoing RPS events in the past few years (Roberts et al. 2021a,b, 2022; Roberts et al. 2022; Ignesti et al. 2022a; Ignesti et al. 2023; Edler et al. 2023).

Observations in the radio continuum are well suited to identify RPS events and trace galaxy SFR. They also allow us to probe the non-thermal phase of the ISM, i.e. the CRE and the magnetic fields via their synchrotron emission. The radio emission of RPS galaxies often appears to be in excess of what is expected given their SFR inferred from observations at other wavelengths (e.g. Gavazzi et al. 1991; Murphy et al. 2009; Vollmer et al. 2010; Chen et al. 2020; Ignesti et al. 2022b,a). Several explanations for the radio-excess of cluster SF-galaxies have been discussed in the literature: Gavazzi & Boselli (1999) proposed that the ram-pressure leads to a compression of the magnetic field and consequentially, increased synchrotron luminosity. Völk & Xu (1994) and Murphy et al. (2009) favored a scenario where the higher radio luminosity is not simply caused by compression, but instead due to shocks driven into the ISM by collisions with fragments of cold gas present in the ICM. Diffusive shock acceleration can then accelerate CRE in the ISM, which should result in a flatter radio spectral index. A third explanation of the radio-excess was brought up more recently in Ignesti et al. (2022a) and Ignesti et al. (2022b) based on the analysis of so-called jellyfish galaxies which are the most extreme examples of galaxies undergoing strong RPS events. The strong radio-excess compared to the H $\alpha$ -emission was interpreted as the consequence of a rapid quenching of the star-forming activity due to RPS. While the H $\alpha$ -emission is a nearly instantaneous SF-tracer, with a typical delay of only a few Myr, the radio-emitting CRE have a typical lifetime > 100 Myr. Thus, if the star formation is quenched on time-scales shorter than the CRE lifetime, we will observe an apparent excess of radio emission simply due to the different time-scales probed by H $\alpha$  and the radio observations. As a consequence, the spectral index of those objects should be rather steep owing to spectral aging.

This work is part of the VIRgo Cluster multi-Telescope Observations in Radio of Interacting galaxies and AGN (ViCTORIA) project, a broadband radio imaging campaign of the Virgo cluster (de Gasperin et al. in prep.). In Edler et al. (2023), we recently published a 144 MHz survey of the Virgo cluster region using the LOFAR high-band antenna system as first data release of ViCTORIA. The survey led to the radio detection of 112 cluster members, with 19 objects that show signs of RPS in their radio morphology. We will use this data set to study the RPS phenomenon in the Virgo cluster.

In this work, we assume a flat  $\Lambda$ CDM cosmology with  $\Omega_m = 0.3$  and  $H_0 = 70 \text{ km s}^{-1} \text{ Mpc}^{-1}$ . At the distance of M87, for which we adopt a value of 16.5 Mpc (Mei et al. 2007; Cantiello et al. 2018), one arcsecond corresponds to 80 pc. This paper is arranged as follows: In Sect. 2, we report the data used for this work and our samples. In Sect. 3, we present a statistical study of the radio and star-forming properties and in Sect. 4, we carry

out a spatially resolved analysis of the LOFAR maps. Finally, our conclusions are outlined in Sect. 6.

## 2. Data and sample

This paper builds primarily on the LOFAR HBA Virgo Cluster Survey (Edler et al. 2023) published as part of the ViCTORIA-project. This 144 MHz-survey covers a 132 deg<sup>2</sup> field around the Virgo cluster and is to date the deepest blind radio continuum survey of this particular region.

### 2.1. RPS sample

For our LOFAR-study of star-forming galaxies in the Virgo cluster, we composed a sample of objects detected in Edler et al. (2023) that show signs of RPS in the radio-continuum. As criteria, we require an asymmetric radio morphology in combination with an undisturbed optical appearance. The latter is to exclude cases where the dominant perturbing mechanism is tidal interaction. If the available literature clearly shows that an object suffers both from tidal interactions and RPS, we include it in our sample. This is the case for NGC 4254 (Vollmer et al. 2005), NGC 4438 (Vollmer et al. 2005) and NGC 4654 (Vollmer 2003). The Virgo cluster has been the target of several multi-frequency surveys and dedicated studies of individual objects. Out of the 19 galaxies with evident tails in radio continuum, 15 were already identified as suffering a RPS event in these detailed studies, as summarized in Boselli et al. (2022). They show tails of stripped atomic or ionized gas, have truncated gaseous and star-forming discs, and have been identified as suffering a RPS event from tuned models and hydrodynamic simulations. Four of the objects are for the first time reported to be RPS candidates based on our LOFAR data: IC 800 shows a radio tail to the northeast, in agreement with being on a radial orbit towards the cluster center, and is strongly H I deficient. IC 3258 is a dwarf galaxy with a radio tail that is also in agreement with a highly radial orbit. NGC 4607 shows a mild asymmetry with an extension of the radio contours towards the northeast and a strong gradient in the opposite direction, it is also highly deficient in neutral hydrogen. Lastly, NGC 4634 shows a radio tail towards the west and is slightly deficient in H I, a star-forming object is coincident with the radio tail (Stein et al. 2018). Preliminary images from the ViCTORIA MeerKAT Survey confirm the morphological peculiarities found in LOFAR for all four objects. For four other galaxies in our RPS sample (IC 3105, IC 3476, NGC 4302 and NGC 4424), the impact of RPS was previously observed at other wavelengths (Chung et al. 2007; Boselli et al. 2021, 2022) but not in the radio continuum.

Since our analysis focuses on the star-forming properties, radio emission due to active galactic nucleus (AGN) activity is a strong contamination. Thus, we investigate the possible contribution of AGN-emission for the galaxies that show signs of ram-pressure stripping in the radio continuum. Three of those objects, NGC 4388, NGC 4438 and NGC 4501 are Seyfert-galaxies. The first two have a radio-morphology that is clearly dominated by nuclear emission (Hummel & Saikia 1991). However, in NGC 4501, the nuclear point-source accounts for only 1% of the total radio emission. The other galaxies mostly host H II-nuclei in the BPT (Baldwin, Phillips & Terlevich; Baldwin et al. 1981) and WHAN ( $W_{\text{H}\alpha}$  versus  $N_{\text{H}}/\text{H}\alpha$ ; Cid Fernandes et al. 2011) diagrams according to Gavazzi et al. (2018). Exceptions are NGC 4302, NGC 4548 and NGC 4569 and which have a nuclear WHAN classification as AGN and an inconclusive nuclear BPT classification. NGC 4607 is also classified as AGN

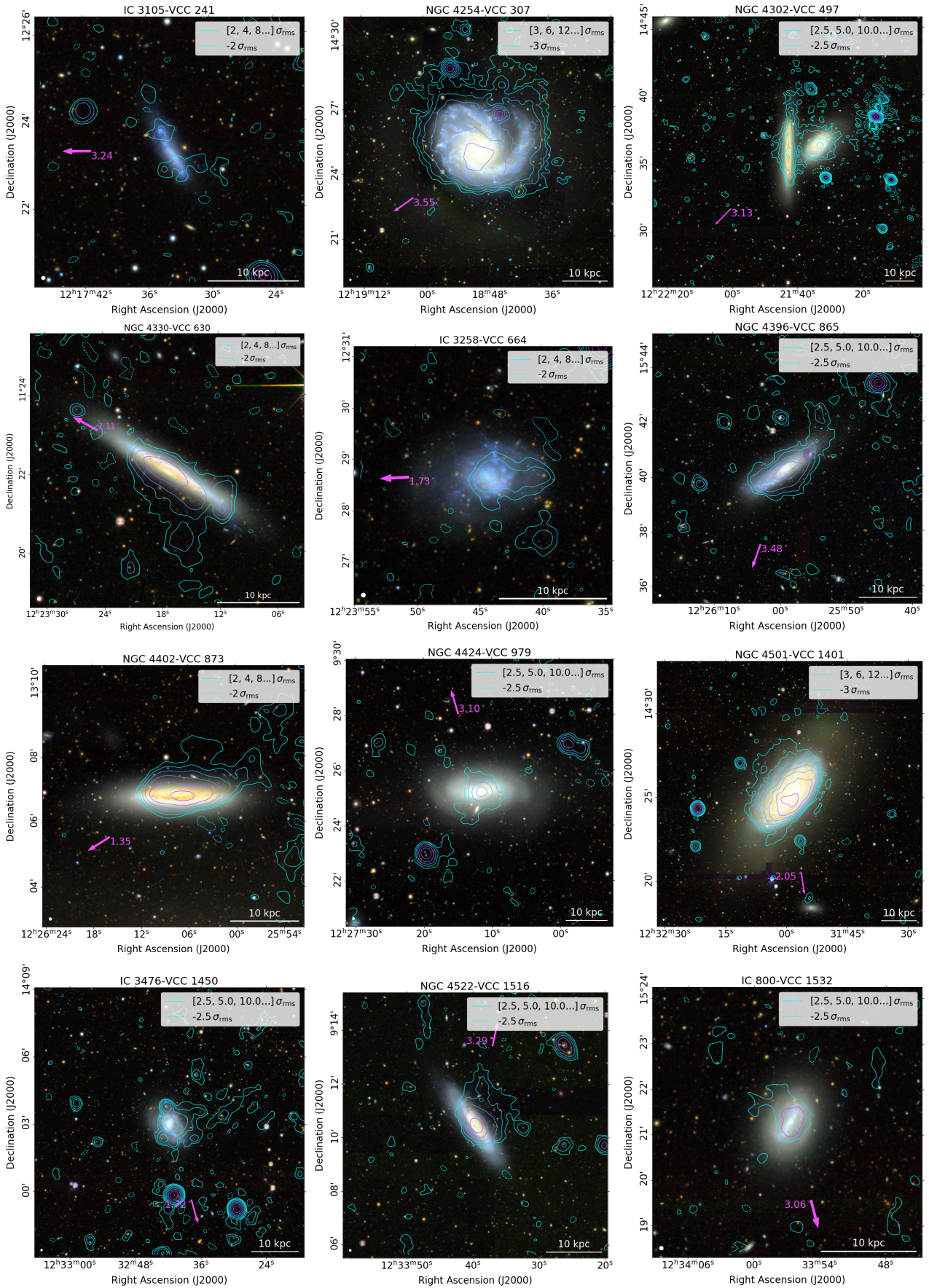


Fig. 1: Radio continuum emission in galaxies with a radio-morphology indicative of RPS. We show LOFAR radio continuum intensity contours at 144 MHz from the 20''-resolution maps overlaid on top of optical images from the DESI Legacy Survey. Contour-levels increase in increments of powers of two and pink arrows indicate the direction and angular distance (in units of degree) to the center of the Virgo cluster.

Table 1: LOFAR sample of ram-pressure stripped galaxies in the Virgo cluster.

VCC	NGC	IC	Morphology	$\log M_\star$ [ $\log M_\odot$ ]	H I-def.	$\Delta v_{\text{rad}, M87}$ [km/s]	Literature	Comment
(1)	(2)	(3)	(4)	(5)	(6)	(7)	(8)	(9)
241		3105	SW tail	7.89	0.41	-1439	B22	new radio tail, H $\alpha$ tail
307	4254		N tail	10.39	0.06	1124	V05, H07, V12b, B18a, M09	RPS + tidal interaction
497	4302		light N tail	10.44	0.50	-153	C07, V13, W12	new radio tail, H I tail
630	4330		S tail	9.52	0.92	321	C07, M09, V12a, V12b, V13, F18	H I tail, H $\alpha$ tail
664		3258	W tail	8.20	0.57	-1713		new candidate
865	4396		NW tail	9.25	0.20	-1398	C07, V07, V10, M09	H I tail
873	4402		NW tail	10.04	0.83	-1049	CR05, V07, M09, V10, V12b	H I tail, stripped dust
979	4424		small S tail	10.17	0.98	-842	C07, V13, B18b	H I tail, H $\alpha$ tail/outflow, radio deficient
1401	4501		NE tail	10.98	0.58	999	W07, V07, V10, V12b	
1450		3476	long W tail	9.02	0.66	-1112	B21	new radio tail, H $\alpha$ tail M87 side-lobes
1516	4522		long NW tail	9.38	0.68	1037	V04, M09, V12b	
1532		800	NE tail	9.07	1.00	1051		new candidate
1615	4548		N-S asymmetry	10.74	0.94	-802	V99, W07	old stripping event
1690	4569		SW tail, outflows	10.66	1.05	-1503	M09, V12b, B16	H $\alpha$ tail
1868	4607		asymmetry	9.60	1.20	973		new candidate
1932	4634		SW tail	9.57	0.45	-1163	S18	new candidate, star-forming object in the tail (S18)
1987	4654		asymmetry	10.14	-0.05	-240	V03, V07, C07, W07, V10	H I tail, RPS and tidal interaction

**Notes.** Columns 1 to 3 list the identifiers of the galaxies in the VCC, NGC and IC. Column 4 comments on the LOFAR morphology of the sources and columns 5 to 7 show the stellar mass (from [Boselli et al. 2015](#)), H I-deficiency (from [Boselli et al. \(2014a\)](#) and [Köppen et al. \(2018\)](#)) and the radial velocity relative to M 87 (taken from HyperLeda<sup>a</sup>). In columns 8 and 9, we list the relevant literature and additional comments.

**References.** V99 – [Vollmer et al. \(1999\)](#); – [Vollmer \(2003\)](#); [Vollmer et al. \(2004\)](#) – V04; CR05 – [Crowl et al. \(2005\)](#); V05 – [Vollmer et al. \(2005\)](#); C07 – [Chung et al. \(2007\)](#); H07 – [Haynes et al. \(2007\)](#); W07 – [Weżgowiec et al. \(2007\)](#); V07 – [Vollmer et al. \(2007\)](#); M09 – [Murphy et al. \(2009\)](#); V10 – [Vollmer et al. \(2010\)](#), V12a – [Vollmer et al. \(2012\)](#); V12b – [Vollmer et al. \(2012\)](#), W12 – [Weżgowiec et al. \(2012\)](#); V13 – [Vollmer et al. \(2013\)](#); B16 – [Boselli et al. \(2016\)](#); B18a – [Boselli et al. \(2018a\)](#); B18b – [Boselli et al. \(2018\)](#); S18 – [Stein et al. \(2018\)](#); B21 – [Boselli et al. \(2021\)](#); B22 – [Boselli et al. \(2022\)](#).

<sup>a</sup> <https://leda.univ-lyon1.fr/>

in the WHAN diagram and as LINER (Low Ionization Nuclear Emission-line Region; [Heckman 1980](#)) or transition object in the BPT, but has an integrated classification as an H II-galaxy. Of those, only NGC 4569 shows a compact nuclear source in the LOFAR maps. While a minor contribution of an AGN cannot be ruled out for this object, this central source is dominantly fueled by nuclear star formation giving rise to prominent outflows ([Boselli et al. 2016](#)). Thus, the only AGN we remove from our sample are NGC 4388 and NGC 4438.

We are left with a sample of 17 RPS galaxies (see [Tab. 1](#)). Their 20''-resolution LOFAR contours on top of the optical images of the Dark Energy Spectroscopic Instrument (DESI) Legacy Survey data release 10 ([Dey et al. 2019](#)) are displayed in [Fig. 1](#). They range from galaxies with clear and prominent 144 MHz tails, such as NGC 4330, NGC 4396, NGC 4522 or IGC 3476 to objects with only mild asymmetry like NGC 4548 and NGC 4607. With the availability of high-sensitivity images of the nearby Virgo cluster, we start probing the regime of dwarf galaxies with radio continuum tails by detecting lower mass systems, down to a stellar mass of  $M_\star = 7.8 \times 10^7 M_\odot$ . Previous studies of more distant clusters and groups are limited to objects with masses  $M_\star \geq 10^9 M_\odot$  ([Roberts et al. 2021a,b, 2022](#); [Ignesti et al. 2022a](#)).

A number of galaxies that were reported in the literature to suffer from RPS ([Boselli et al. 2022](#)) are not part of our LOFAR RPS sample. Of those, IC 3412, IC 3418, NGC 4506 and UGC 7636 are non-detections in LOFAR at  $4\sigma$ . Others, mostly galaxies which have tails in H I, are radio-detected but show a symmetric radio morphology. Those objects are NGC 4294, NGC 4299, NGC 4469, NGC 4470, NGC 4491 and NGC 4523

([Chung et al. 2007](#); [Boselli et al. 2023b](#)). For these objects, we speculate that they experience rather mild ram-pressure, which mostly affects the outskirts of the ISM, such that a tail in radio continuum is below our sensitivity threshold. Alternatively, the peculiar H I morphology of these objects could be due to other process than RPS. In the case of NGC 4470, the non-detection of a continuum tail is due to local dynamic range limitations in the LOFAR map, indeed preliminary images of our ViCTORIA MeerKAT survey reveal a prominent tail at 1.3 GHz. For NGC 4523, a continuum counterpart to the H I tail which we reported in [Boselli et al. \(2023b\)](#) is also observed in the preliminary MeerKAT maps, although at low significance.

## 2.2. LOFAR-HRS sample

To assess how the non-thermal properties of galaxies in the Virgo cluster are shaped by their local surroundings, we compile a comparison sample of nearby galaxies with high-quality star formation tracer data available. For this, the Herschel Reference Survey (HRS; [Boselli et al. 2010](#)), which also contains all but two of the galaxies in our RPS sample, is well suited. This survey consists of a statistically complete, K-band limited sample of 323 nearby (15–25 Mpc distance) galaxies. Around a quarter of those galaxies reside in the Virgo sub-clusters around either M 87 or M 49, another quarter is located in other sub-structures of the Virgo cluster or its outskirts. The remaining objects are in less dense environments such as groups and pairs or are isolated galaxies. This allows us to compare the properties of galaxies in the Virgo cluster with those that are inhabiting poorer surroundings.

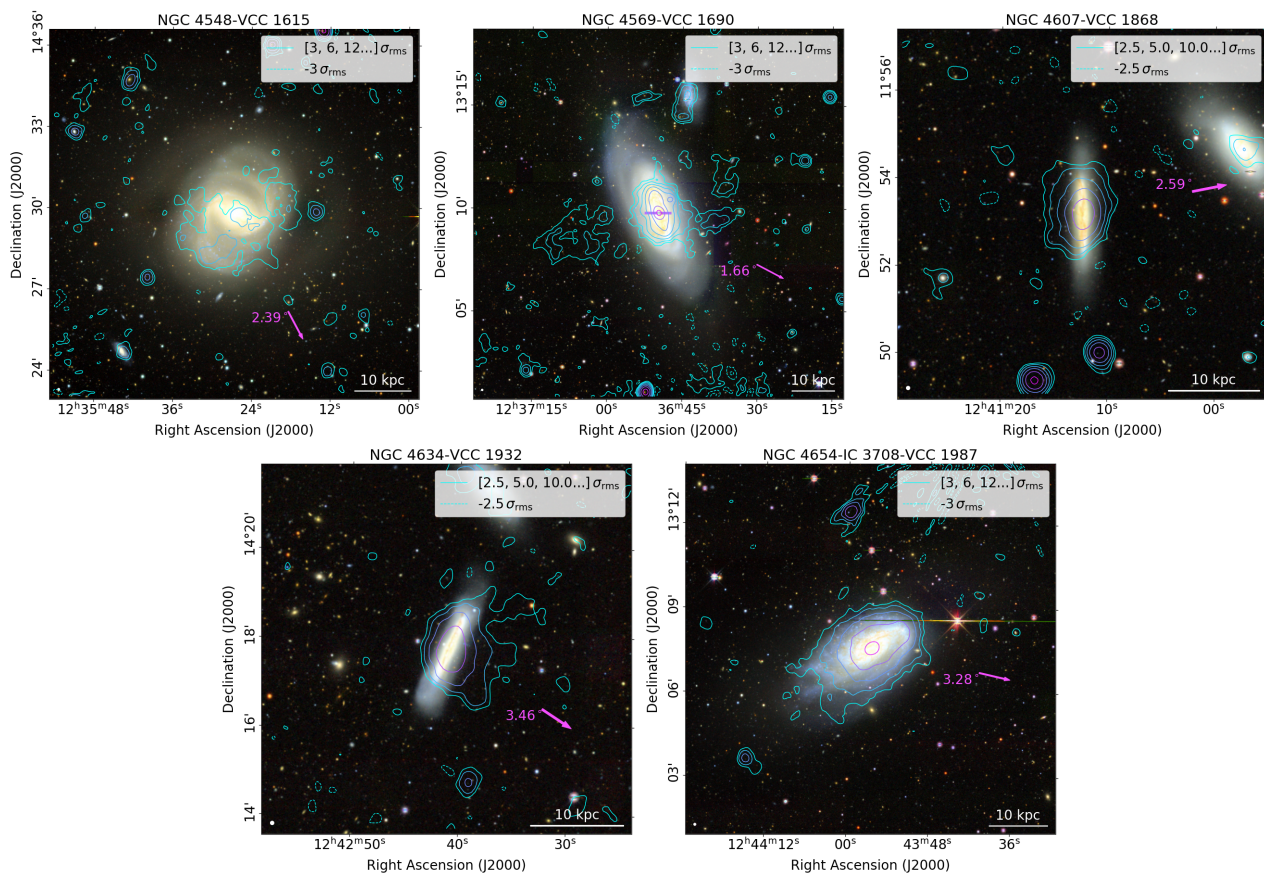


Fig. 1: Continued.

We construct a sample of the 144 MHz LOFAR-detected star-forming galaxies in the HRS. For this, we use data of the LOFAR HBA Virgo Cluster Survey (Edler et al. 2023), which covers the majority of the galaxies in the Virgo Cluster. In addition, all the HRS galaxies at declinations of  $\delta > 30^\circ$  are covered by the second data release of the LOFAR Two-metre Sky Survey (LoTSS-DR2; Shimwell et al. 2022). Further galaxies were observed by more recent, previously unpublished observations of LoTSS, processed by the LOFAR Surveys Key Science Project<sup>1</sup>. All LOFAR HBA observations were taken with identical observational settings and processed using the ddf-pipeline algorithm (Tasse et al. 2021). For the Virgo cluster observations, additional pre-processing was necessary due to the close proximity to the extremely luminous radio galaxy M87 (Virgo A), those steps are described in Edler et al. (2023).

For the HRS galaxies in the footprint of the LOFAR HBA Virgo Cluster Survey, we use the 144 MHz measurements reported in Edler et al. (2023) based on the 20''-resolution LOFAR-maps. In this paper, all HRS galaxies within the survey area were considered. We extend this sample also to the HRS galaxies covered by LoTSS-DR2 as well as to those which are within 1.97° angular distance of unpublished LoTSS-observations processed before August 2023. We manually inspect all HRS galaxies in the LoTSS 20''-maps and, if they are visible in the radio images, we measure the flux density in a region encompassing the  $3\sigma$ -contours as it was done in Edler et al. (2022) for the Virgo objects. For observations outside of LoTSS-DR2, we use the pointing closest to the galaxy of interest and we take into account a field-dependent factor to align

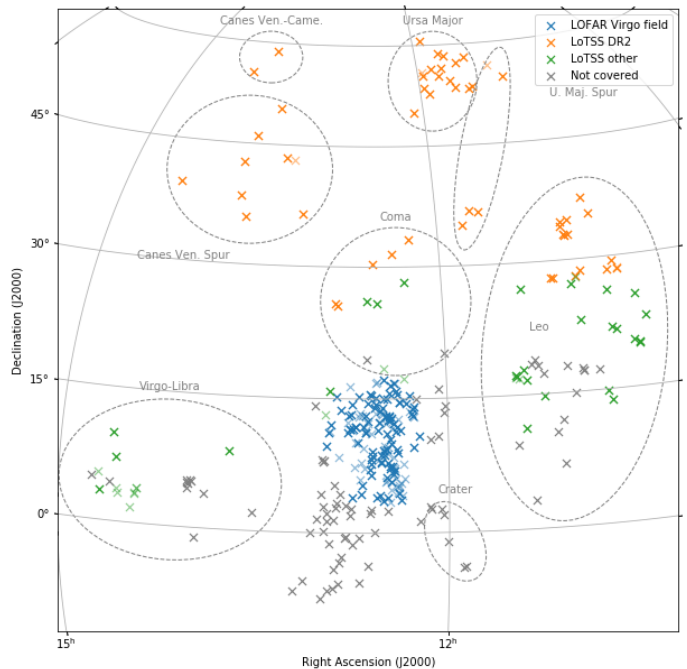


Fig. 2: LOFAR-coverage of the HRS. The galaxies are either in the LOFAR Virgo Cluster Survey (blue), in LoTSS-DR2 (orange) or covered in further LoTSS observations (green). Grey crosses are not covered by LoTSS, and colored but partially transparent points are covered but not detected. Dashed regions mark structures of galaxies other than the Virgo cluster.

<sup>1</sup> <https://lofar-surveys.org/>

the flux density scale with the one of the 6 C-survey (Hales et al. 1988) and NRAO VLA Sky Survey (NVSS; Condon et al. 1998). This factor was calculated as described in Shimwell et al. (2022). We consider all galaxies with an integrated signal-to-noise ratio above four as radio-detected. While we use the 10% systematic uncertainty of the flux density scale for LoTSS-DR2 as reported in (Shimwell et al. 2022), a larger uncertainty of 20% is assumed for the other LOFAR maps due to the reduced overlap and statistics, the higher uncertainty of the primary beam model for low declinations, and the presence of bright sources such as M 87 (for sources in the Virgo field, Edler et al. (2023)). In Fig. 2, we show the sky distribution of the HRS galaxies and their coverage by the different LOFAR projects. In total, out of the 261 late-type galaxies in the statistically complete sample of the HRS (excluding ellipticals and lenticulars), 193 are in the footprint of our LOFAR observations. Of those, 141 galaxies are detected, 76 are in the LOFAR Virgo field, 44 are from LoTSS-DR2, and 21 are in LoTSS-fields outside of the LoTSS-DR2 footprint.

Since we are interested in radio emission as tracer of the SFR, we need to exclude objects where a significant fraction of the radio emission is due to an active galactic nucleus (AGN). By excluding elliptical and lenticular galaxies, we remove most objects with strong AGN contamination. In Gavazzi et al. (2018), nuclear spectroscopy-based BPT and WHAN classifications for the HRS galaxies were presented. Eleven of the LOFAR-detected objects were classified as either strong or weak AGN in the WHAN diagram and as Seyfert galaxy in the BPT diagram. Visually inspecting the radio maps of those revealed that for six of them the nuclear point-like sources contribute >15% to the flux density. These objects (NGC 3227, NGC 4313, NGC 4419, NGC 4586) were removed from our sample. All galaxies in the RPS sample described in Sect. 2.1 except for IC 3105 and IC 3258, which are fainter than the limiting  $K$ -band magnitude of 12, are also part of the HRS. Those two objects will also be part of our analysis but are excluded from any fitting since they do not meet the selection criteria of the HRS. In the following, we will refer to the objects in our LOFAR-HRS sample minus the objects in our RPS sample for simplicity as the non-RPS sample.

In Appendix A, we display the 144 MHz measurements of the 137 LOFAR-detected star-forming galaxies used in this work. The spectral luminosity  $L_{144}$  at 144 MHz is calculated from the measured flux densities  $S$  according to  $L_{144} = 4\pi d^2 S$ ; since our sample only consists of nearby galaxies at  $v < 1750 \text{ km s}^{-1}$ , we neglect  $k$ -correction. We employed distances  $d$  following the HRS (Boselli et al. 2010), with the difference that we set the distance to objects in the Virgo cluster to 16.5 Mpc instead of 17 Mpc to be consistent with what was assumed in the NGVS (Ferrarese et al. 2012) and VESTIGE (Boselli et al. 2018b).

### 2.2.1. Star formation tracers

The integrated radio luminosities serve as a tracer of the SFR of the individual galaxies in the sample. A key advantage of radio-inferred SFR is that it is not affected by dust-attenuation (Condon 1992; Murphy et al. 2011). Thus, no extinction-correction is required. While at low radio frequencies, the radio emission is almost free from the Bremsstrahlung-contribution of thermal electrons, the synchrotron lifetime of CRe in a magnetic field  $B$  (Beck & Krause 2005):

$$t_{\text{syn}} = 88 \text{ Myr} \left( \frac{B}{10 \mu\text{G}} \right)^{-3/2} \left( \frac{\nu}{144 \text{ MHz}} \right)^{-1/2} \quad (1)$$

is longer compared to CRe probed at higher frequencies. So an underlying assumption of SFRs derived from low frequency observations is that the SFR is constant on timescales of  $\approx 100 \text{ Myr}$ .

To compare the radio luminosity to further tracers of the star-forming activity, we consider SFRs based on far-UV (FUV) and H $\alpha$ . The SFRs obtained from H $\alpha$  and FUV were reported in Boselli et al. (2015) for the HRS star-forming galaxies based on the Salpeter initial mass function (IMF) and the calibration of Kennicutt (1998). We converted the SFR to a Chabrier IMF (Chabrier 2003) by applying a factor of 0.63 to the SFRs (Madau & Dickinson 2014). The SFRs also need to be corrected for dust attenuation. For the UV-based SFR, Boselli et al. (2015) employed a correction based on the  $24 \mu\text{m}$  emission. For the H $\alpha$ -inferred SFR, two approaches were compared in Boselli et al. (2015) – a correction based on the Balmer-decrement using spectroscopic data (Boselli et al. 2013) and a method relying on the  $24 \mu\text{m}$  dust emission. The authors found that the correction with the Balmer decrement  $C(H\beta)$  as defined in Lequeux et al. (1981) is only accurate if the fractional uncertainty is  $\sigma[C(H\beta)] < 0.1$ ; on the other hand, the correction using the  $24 \mu\text{m}$  emission can be biased for systems with a particularly low specific SFR due to the contribution of the old stellar population to the dust heating (Cortese et al. 2008; Boselli et al. 2015). Thus, we use the values corrected with the Balmer-decrement if  $\sigma[C(H\beta)] < 0.1$ , and with the  $24 \mu\text{m}$  emission otherwise.

No uncertainty estimates are available for the SFRs published in Boselli et al. (2015). In the following, we assume a systematic uncertainty of 15% for the GALEX UV measurements (Gil de Paz et al. 2007) and the H $\alpha$  photometry with the San Pedro Martir telescopes (Boselli et al. 2015, 2023a). We neglect the photometric uncertainty of the Spitzer  $24 \mu\text{m}$  measurements used for a dust correction as they have a uncertainty of only 2% (Engelbracht et al. 2007). We note that those estimates are only a rough first-order approximation of the true uncertainties, which also would require us to take into account the complex and hardly quantifiable dependencies on the dust and N II-line corrections and the SFR conversion (for discussions of those, see e.g. Boselli et al. 2015, 2016, 2023a). We ensure that the SFRs are based on the same distances as the radio luminosities by re-scaling the SFRs by  $(d/d_{\text{HRS}})^2$ .

Another common SFR-tracer is the infrared-emission which traces the dust heated by the young stellar population. As already mentioned, in systems with low specific SFR, older stellar populations also contribute to the dust heating. Low specific SFR systems are systematically more common in our sample which includes relatively quenched galaxies in the Virgo cluster (Boselli et al. 2016). For this reason, we do not consider SFRs based purely on the infrared emission.

### 2.2.2. Sample properties

The stellar masses of our sample were obtained from Cortese et al. (2012) who used the Chabrier IMF and span a large regime, ranging from  $3.0 \times 10^8 M_{\odot}$  to  $1.3 \times 10^{11} M_{\odot}$ . The two additional RPS galaxies outside of the HRS, IC 3105 and IC 3258, are of even lower mass with  $M_{\star} = 7.8 \times 10^7 M_{\odot}$  and  $M_{\star} = 8.3 \times 10^7 M_{\odot}$ , respectively. In Fig. 3, the mean of the H $\alpha$  and UV-based SFR is shown as a function of the stellar mass. We also display the star-forming main sequence relation for Virgo cluster galaxies with normal H I-content (Boselli et al. 2023a). As RPS generally reduces the SFR, RPS galaxies are expected to mostly lie below this relation. In some cases, RPS galaxies can show a high specific SFR due to a temporary enhancement of SFR (Bothun & Dressler 1986; Vulcani et al. 2018; Roberts & Parker

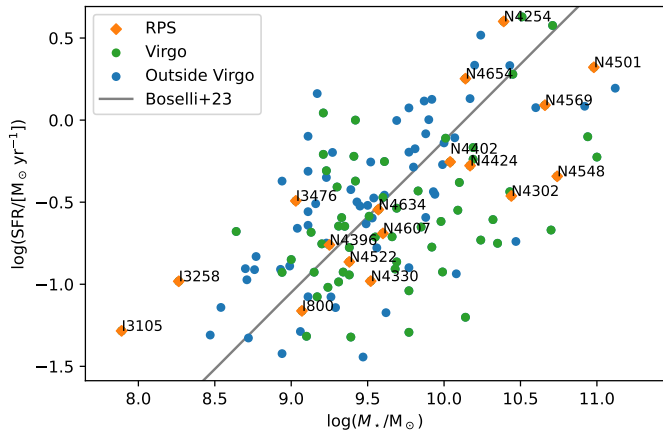


Fig. 3: SFR (mean of  $H\alpha$  and UV-based values) as function of stellar mass for galaxies in the RPS sample (orange diamonds), galaxies in the Virgo cluster region (within  $10^\circ$  from M 87, green circles) and galaxies outside of the cluster (blue circles). For comparison, we show the star-forming main sequence for Virgo cluster galaxies with normal H I-content (Boselli et al. 2023a, grey line).

2020). Since our sample is limited to 144 MHz detected objects, we are biased towards high-SFR objects, in particular at the low-mass end of the distribution.

### 3. Statistical analysis

#### 3.1. Radio-SFR-relation

The availability of radio and other SFR-tracers for our data allows us to investigate the radio-SFR-relation for our samples. Particularly at low radio-frequencies, this radio-SFR-relation is known to deviate from the linear scenario (Heesen et al. 2022). Thus, we fit a power-law relation of the form:

$$\left(\frac{L_{144}}{\text{W Hz}^{-1}}\right) = N_0 \left(\frac{\text{SFR}}{\text{M}_\odot \text{yr}^{-1}}\right)^\beta. \quad (2)$$

Fitting is performed in log-log space, where the expression assumes a linear form. We use the orthogonal method of the *bivariate errors and intrinsic scatter* (BCES) regression algorithm (Akritas & Bershady 1996; Nemmen et al. 2012) for the minimization.

We fitted Eq. 2 for the  $H\alpha$  and UV inferred SFRs and for the HRS galaxies in the RPS sample and those not in the RPS sample independently. The scatter  $\sigma_{\text{raw}}$  of the data points around the fit is calculated as:

$$\sigma_{\text{raw}}^2 = (n - 2)^{-1} \sum_i (\log L_{144,i} - \beta \log \text{SFR}_i - \log N_0)^2, \quad (3)$$

where  $n$  is the sample size. The best-fitting parameters are reported in Tab. 2 and we display the fit results together with the data points in Fig. 4.

For both SFR tracers, the relation for the radio continuum luminosity derived for the RPS sample is a factor of 2–3 above the one found for the non-RPS galaxies. This is expected given the reports of enhanced radio-to-SFR ratios for RPS galaxies in the literature (Murphy et al. 2009; Vollmer et al. 2010, 2013; Roberts et al. 2021a; Ignesti et al. 2022a). In Fig. 4, we also display the relations derived from LOFAR observations of SF-galaxies in other works: Heesen et al. (2022) analyzed a sample

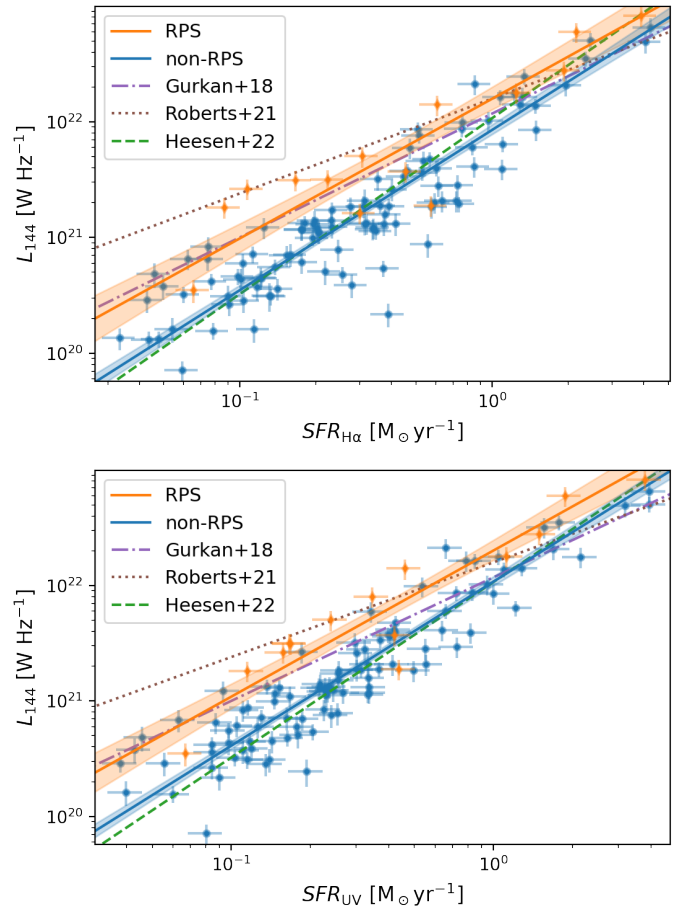


Fig. 4: Radio-SFR relations. Top panel:  $H\alpha$ -inferred SFRs against radio luminosity for galaxies in the RPS sample (orange data points) and other galaxies in the LOFAR HRS sample (blue data points). The orange and blue lines represent the best-fitting power-law fits and the corresponding  $1\sigma$  uncertainty bands for those samples. The green, purple and brown lines are fits taken from the literature. Bottom panel: Same as above but for the UV-based SFRs.

of 45 nearby galaxies, Gürkan et al. (2018) studied a sample of  $> 2000$  SF-galaxies across a wide range of redshifts and Roberts et al. (2021a) published a relation for a sample of 95 jellyfish galaxies in low-redshift clusters.

#### 3.2. Mass dependency and radio excess

The resulting power-law fits for our samples are super-linear with  $\beta \approx 1.4$ . This super-linearity is thought to originate from a mass-dependence in the calorimetric efficiency  $\eta = \eta(M)$ , which is the ratio of CRE energy that is radiated within galaxy. In larger galaxies with a higher mass  $M$ , CRE have longer escape times  $t_{\text{esc}}$  in relation to their lifetime  $t_{\text{syn}}$ , thus, they lose a greater fraction of their energy inside the galaxy before escaping into regions with low magnetic field strengths.

We use the following parametrization to enforce a linear radio-SFR relation while taking into account a mass-dependent calorimetric efficiency (see e.g. Heesen et al. 2022):

$$L_{144} = N_0 \left(\frac{\text{SFR}}{\text{M}_\odot \text{yr}^{-1}}\right) \left(\frac{M_\star}{10^{10} \text{M}_\odot}\right)^\gamma. \quad (4)$$

Table 2: Best-fitting parameters for different parametrizations of the radio-SFR relation.

Tracer	Sample	$N_0 [10^{21}]$	$\beta$	$\gamma$	$\sigma_{\text{raw}}$	$n$
H $\alpha$	RPS	$15.8 \pm 2.1$	$1.21 \pm 0.11$	–	0.28	14
H $\alpha$	others	$8.5 \pm 0.67$	$1.39 \pm 0.06$	–	0.28	103
UV	RPS	$20.0 \pm 2.6$	$1.27 \pm 0.11$	–	0.23	14
UV	others	$10.8 \pm 0.8$	$1.42 \pm 0.06$	–	0.24	102
H $\alpha$	RPS	$13.7 \pm 2.5$	–	$0.08 \pm 0.13$	0.29	14
H $\alpha$	others	$7.2 \pm 0.6$	–	$0.23 \pm 0.05$	0.27	103
UV	RPS	$16.0 \pm 2.5$	–	$0.08 \pm 0.12$	0.26	14
UV	others	$7.8 \pm 0.5$	–	$0.21 \pm 0.04$	0.25	102
H $\alpha$	RPS	$14.1 \pm 3.6$	$1.05 \pm 0.25$	$0.05 \pm 0.21$	0.29	14
H $\alpha$	others	$8.3 \pm 0.7$	$1.22 \pm 0.06$	$0.12 \pm 0.06$	0.26	103
UV	RPS	$20.3 \pm 5.2$	$1.26 \pm 0.23$	$0.09 \pm 0.19$	0.25	14
UV	others	$9.9 \pm 0.8$	$1.28 \pm 0.06$	$0.08 \pm 0.05$	0.24	102

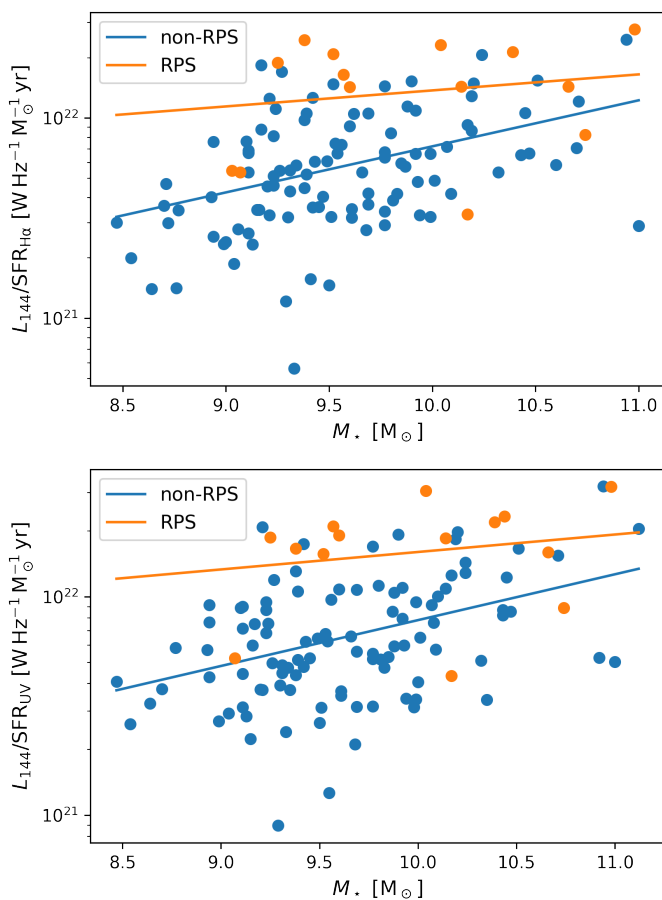


Fig. 5: Top panel: Ratio of  $L_{144}$  to  $\text{SFR}_{\text{H}\alpha}$  as a function of  $M_*$ . The orange data points mark the galaxies in the RPS sample, the blue ones the galaxies outside the RPS sample. The orange and blue lines are the corresponding fits. Bottom panel: Same but for the UV-inferred SFR.

Here,  $\gamma$  describes the dependency on the stellar mass  $M_*$ . We repeat the fitting for the RPS and non-RPS galaxies for both SFR-tracers. The best-fitting model-parameters are reported in Tab. 2, and the data points and fits are shown in Fig. 5. For the galaxies that do not show a RPS-morphology, we can reproduce the systematic increase of  $L_{144}/\text{SFR}$  as a function of mass, finding a positive mass-exponent of  $\gamma \approx .2$ .

Again, the population of RPS galaxies has a clear radio-excess with 12/14 galaxies above the relation for non-RPS galaxies. However, for them, the mass-dependency is less clear. This could be either due to an increased scatter in  $L_{144}/\text{SFR}$  for this population, indirectly connected to the ram-pressure stripping, or due to the small sample size.

We further investigate a relation with an additional free parameter, which is a power-law in both mass and SFR (see Gürkan et al. 2018):

$$\left(\frac{L_{144}}{\text{W Hz}^{-1}}\right) = N_0 \left(\frac{\text{SFR}}{\text{M}_\odot \text{yr}^{-1}}\right)^\beta \left(\frac{M_*}{10^{10} \text{M}_\odot}\right)^\gamma. \quad (5)$$

The best-fitting results for this parametrization are displayed in Tab. 2. For the non-RPS galaxies, we find a mass-exponent of  $\gamma \approx 0.1$  and an SFR-exponent of  $\beta \approx 1.25$ . Those results can be compared to the ones from Gürkan et al. (2018), who found a flatter relation with SFR ( $\beta = 0.77$ ) but a steeper exponent in mass ( $\gamma = 0.44$ ).

To quantify the radio-excess (or deficit) compared to the best fit of Eq. 5 for the non-RPS sample, we calculate the distance of the RPS-galaxies to the best-fitting plane in log-space according to:

$$d_{3D} = \frac{\log\left(\frac{L_{144}}{\text{W Hz}^{-1}}\right) - \beta \log\left(\frac{\text{SFR}}{\text{M}_\odot \text{yr}^{-1}}\right) - \gamma \log\left(\frac{M_*}{10^{10} \text{M}_\odot}\right)}{\sqrt{\beta^2 + \gamma^2 + 1}}. \quad (6)$$

We display those distances in Fig. 6. In general, there is a good agreement between the distances based on the UV and H $\alpha$ -inferred SFR. The only object with a strong radio-deficit is the peculiar galaxy NGC 4424, which is thought to be a merger remnant and shows outflows of ionized gas (Boselli et al. 2018). Similarly, the galaxies with a clear RPS morphology in radio show the strongest radio-excesses, those are NGC 4522, NGC 4330, NGC 4396, NGC 4402 and NGC 4634. Qualitatively, there appears to be a connection between the asymmetry of the radio emission and the strength of the radio excess. The only exception being IC 3476, which shows a strong tail but only a mild excess of  $\approx 10\%$ . Possibly, the radio emission of this source is underestimated due to masked background sources and side-lobes of M 87 which unfortunately cover parts of the tail of this source.

### 3.3. Spectral properties

To probe if the spectral properties of the galaxies in the ram-pressure stripped sample differ from the ones of unperturbed



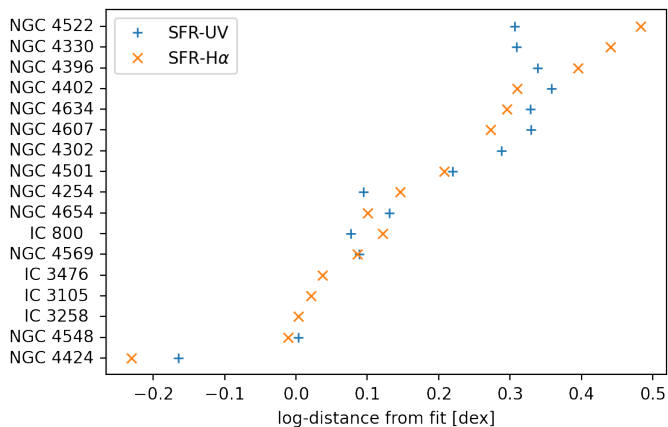


Fig. 6: Distance of the RPS galaxies to the best-fitting  $L_{144}$ -SFR- $M_*$ -plane for the non-RPS galaxies in log-space. The galaxies are sorted by the mean of the  $SFR_{UV}$  and  $SFR_{H\alpha}$  based log-distances.

galaxies, we determined the integrated spectral index  $\alpha^2$  for all objects which have radio-measurements also at 1.4 GHz available in the literature. The spectral index  $\alpha$  between two frequencies  $\nu_1, \nu_2$  with flux density measurements  $S_1, S_2$  is calculated as:  $\alpha = \ln(S_1/S_2)/\ln(\nu_1/\nu_2)$ . We estimate the corresponding uncertainties following Gaussian propagation of uncertainty. The 1.4 GHz flux densities or upper limits were collected from Murphy et al. (2009), Chung et al. (2009) (re-measured in cases where the maps were provided by the authors), Vollmer et al. (2010) and Boselli et al. (2015). For the two RPS objects which are not in the HRS, we derived the  $4\sigma$  upper limits from the NVSS (Condon et al. 1998). To allow for comparison with the work of Heesen et al. (2022), we estimated the total masses of the galaxies in our sample. For this, we employed the dynamical data derived from H $\alpha$  (Gómez-López et al. 2019) or H I (Boselli et al. 2014a) observations according to  $M_{\text{tot}} = r_{\text{SF}} v_{\text{rot}}^2 / G$ , where  $G$  is the gravitational constant,  $v_{\text{rot}}$  the rotation velocity and  $r_{\text{SF}}$  the size of the star-forming disk, estimated from  $D_{24}$  or  $D_{25}$  as described in Gómez-López et al. (2019).

In Fig. 7, we display the total mass-spectral index-distribution of the 114 galaxies with available 1.4 GHz measurements, for the 26 objects without detection, we provide an upper limit. We also show the best-fitting log-linear relation of the form  $\alpha = A \log(M_{\text{tot}}/M_{\odot}) + B$ . For the galaxies outside of our RPS sample, we find  $A = -0.13 \pm 0.02$  and  $B = 0.83 \pm 0.20$ , in excellent agreement with the parameters derived by Heesen et al. (2022) ( $A = -0.13$  and  $B = 0.81$ ). However, for the RPS sample, we find evidence that the relation is shifted towards steeper spectral index values with  $A = -0.06 \pm 0.05$  and  $B = 0.09 \pm 0.52$ . Evaluated at  $M_{\text{tot}} = 3 \times 10^{10} M_{\odot}$ , the relations differ by  $\Delta\alpha = 0.17 \pm 0.06$ . We cross check that this finding is not simply caused by a systematic underestimation in the dynamical estimates of  $M_{\text{tot}}$  due to truncated gas disks in RPS galaxies by repeating the fitting using  $M_*$ , where we find  $\Delta\alpha = 0.13 \pm 0.07$  at  $M_* = 4 \times 10^9 M_{\odot}$ . A strong outlier from the relation is NGC 4548 with a particularly steep spectral index of  $\alpha = -1.3 \pm 0.1$  measured from the VIVA (Chung et al. 2009) map with low image fidelity. However, the  $4\sigma$  upper limit from the NVSS map (Condon et al. 1998) agrees with a steep spectrum  $\alpha \leq -1.0$ . Our finding with a best-fitting relation for the RPS galaxies that is

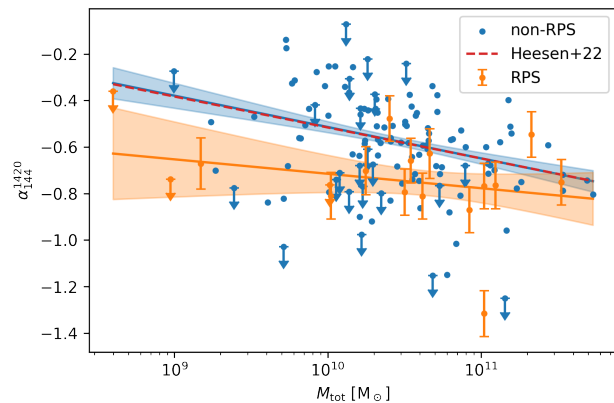


Fig. 7: Total mass against spectral index for the RPS sample (orange markers) and the other galaxies in the sample (blue markers). For clarity, uncertainties are only displayed for the RPS sample, they are of comparable size ( $\sigma_{\alpha} \sim 0.1$ ) for the other galaxies. Downward pointing arrows correspond to  $4\sigma$  upper limits. The orange and blue line show the corresponding best-fitting relations, and the red dashed line shows the fit from Heesen et al. (2022).

shifted to lower values of  $\alpha$  holds when repeating the analysis without NGC 4548 ( $\Delta\alpha = 0.13 \pm 0.04$  at  $M_{\text{tot}} = 3 \times 10^{10} M_{\odot}$ ).

We also investigated if there is a correlation between the spectral index and the log-distance from the best-fitting  $L_{144}$ -SFR- $M_*$  plane for the RPS sample. We find a slightly positive Pearson's correlation coefficient of 0.30 using  $SFR_{UV}$  and 0.377  $SFR_{H\alpha}$ , however, both are not significant ( $p$ -value  $> 0.23$ ), the slightly positive relation is due to the low luminosity steep spectrum source NGC 4548.

#### 4. Spatially resolved radio-SFR analysis

In Sect. 3.2, we showed that the radio emission of our Virgo RPS sample is enhanced up to a factor of 3 compared to the H $\alpha$  and UV-inferred SFR. The localization of this excess allows to constrain the origin of the surplus radio emission. So could a leading-edge enhancement point towards compression of the magnetic field lines or to ram-pressure driven shocks as additional source of CRE. To investigate this, we created maps of the ratio between the observed radio surface brightness  $B_{\text{obs}}$  and the expected radio surface brightness  $B_{\text{model}}$  based on the SFR-surface density  $\Sigma_{\text{SFR}}$ . A similar analysis was carried in Murphy et al. (2009) for six of the galaxies in our sample using 1.4 GHz VLA observations and *Spitzer* far-infrared emission as SFR-tracer. For our analysis, we derived the SFR-surface density from *GALEX* NUV (Martin et al. 2005) following the calibration of Leroy et al. (2019). We employed a dust-correction based on Herschel 100  $\mu\text{m}$  measurements obtained from the HRS (Cortese et al. 2014) and HeVICS (Davies et al. 2010) according to Kennicutt & Evans (2012). Foreground and background sources in the  $\Sigma_{\text{SFR}}$  and LOFAR maps were manually masked and the maps were gridded to the same pixel layout. We convolved the  $\Sigma_{\text{SFR}}$ -maps to match the resolution of our LOFAR maps (either  $9'' \times 9''$  or  $20'' \times 20''$ ) using the convolve method implemented in astropy (Astropy Collaboration et al. 2022). We obtained the model for the radio emission using Eq. 4 and our best-fitting parameters ( $N_0 = 7.7 \times 10^{21}$  and  $\gamma = 0.21$ ) for the non-RPS sample to convert  $\Sigma_{\text{SFR}}$  to the radio surface bright-

<sup>2</sup> Defined as  $S \propto \nu^{\alpha}$ .

ness  $B$ :

$$\frac{B_{\text{model}}}{\text{Jy beam}^{-1}} = \frac{N_0}{4\pi \times 10^{-26}} \left( \frac{\Sigma_{\text{SFR}}}{\text{M}_{\odot} \text{ yr}^{-1} \text{ kpc}^2} \right) \left( \frac{M_{\star}}{10^{10} \text{M}_{\odot}} \right)^{\gamma} \left( \frac{A_{\text{beam}}}{\text{kpc}^2} \right)^{-1} \left( \frac{d}{\text{m}} \right)^{-2}. \quad (7)$$

Since the CRe have lifetimes of  $\sim 100$  Myr and are subject to CR-transport, the synchrotron emission of an undisturbed galaxy should be a smoothed version of SFR-surface density (e.g. Heesen et al. 2023a), this can be expressed in terms of the CRe-transport length  $l_{\text{CRe}}$ . The shape of the smoothing kernel used to model the CR-transport depends on the transport process. We assume as a benchmark the case of pure diffusion modeled by a Gaussian kernel. The width  $\sigma$  of the Gaussian kernel used for the smoothing is related to  $l_{\text{CRe}}$  according to  $\sigma = (2\ln 2)^{-0.5} l_{\text{CRe}}$ .

Since CRe diffuse away from the star-forming regions into regions with low or no star-forming activity, the resolved  $B$ - $\Sigma_{\text{SFR}}$ -relation is sub-linear, opposite to the global radio-SFR-relation. Taking into account CRe diffusion with an appropriate choice of  $l_{\text{CRe}}$ , the relation can be linearized (Murphy et al. 2009; Berkhuijsen et al. 2013; Heesen et al. 2023a). To linearize this relation, we fit the convolution kernel size  $\sigma$ . For each  $\sigma$ , we determine the slope  $a$  of the relation by fitting the pixels that are above a signal-to-noise ratio of 5 in both maps. Due to their low surface brightness, we instead require a S/N of 3 for IC 800 and IC 3105 and 4 for NGC 4548. The optimal  $\sigma$  is found once the slope reaches unity. We carried out the smoothing procedure based on maps at  $9''$  resolution (for sources with sufficient surface brightness) and at  $20''$  resolution. The resulting transport lengths are listed in Tab. 3, there is decent agreement between the values derived at different resolutions. Two notable outliers with a large transport length are NGC 4254 and NGC 4548 with  $l_{\text{CRe}} > 5$  kpc. Those values are larger than the values  $\leq 3.8$  found for field galaxies at 144 MHz in Heesen et al. (2023b). This is likely due to the significant contribution of the external perturbations to the CRe-transport, a scenario also suggested by Ignesti et al. (2022b).

We then convolved the maps of the model surface brightness using a Gaussian kernel with the corresponding width  $\sigma$ . In Fig. 8, we display the log-ratio  $R = \log_{10}(B_{\text{obs}}/B_{\text{model}})$  between the observed and the modeled radio emission for all pixels with a signal-to-noise ratio above 3 (above 2 in the case of IC 3105). We also mark the  $5\sigma$  contours of the SFR-surface density and radio surface brightness. For sufficiently bright sources, we used the  $9''$ -resolution maps to derive the ratios, otherwise the  $20''$ -resolution ones. For the former, we present the  $20''$  maps, which are more sensitive to the faint tails, in Appendix B.

In general, the radio excess is a global phenomenon and all galaxies but NGC 4424, NGC 4548 and IC 3258 show enhanced radio emission across the disk. As expected, the excess is strongest at the trailing edge or in the tail, where all objects show some form of enhanced radio emission or radio contours that extend asymmetrically beyond the SFR contours at the trailing edge. This is most pronounced in NGC 4330, NGC 4522 and NGC 4634, while NGC 4548 shows only a mild enhancement in parts of the trailing half of the disk. The reason for the excess radio emission in the tails is the advection of CRe from the disk due to RPS to regions with low star-forming activity (e.g. Murphy et al. 2009; Ignesti et al. 2022a). At the same time, many galaxies show a deficit of radio emission at the leading edge (i.e.  $\Sigma_{\text{SFR}}$  contours that extend beyond the radio contours) - e.g. in NGC 4330, NGC 4396, NGC 4402, NGC 4522, NGC 4548 and IC 3476 (see also Murphy et al. (2009)). However, the leading-edge deficit is not omnipresent. Most notably, in NGC 4501, we

instead observe an enhancement of radio emission at the leading edge – likely connected to a local compression of magnetic fields (Vollmer et al. 2008).

Table 3: CRe transport length and spectral indices of the RPS sample.

Name	$l_{\text{CRe}}^{9''}$ [kpc]	$l_{\text{CRe}}^{20''}$ [kpc]	$\alpha_{144 \text{ MHz}}^{1.4 \text{ GHz}}$
IC 3105	–	2.3	$< -0.36^a$
NGC 4254	5.2	5.4	$-0.77 \pm 0.10^b$
NGC 4302	4.4	3.9	$-0.77 \pm 0.10^c$
NGC 4330	1.9	1.1	$-0.63 \pm 0.11^c$
IC 3258	–	1.8	$< -0.74^a$
NGC 4396	2.3	1.3	$-0.79 \pm 0.10^c$
NGC 4402	1.4	1.6	$-0.81 \pm 0.10^c$
NGC 4424	1.9	1.4	$-0.67 \pm 0.11^c$
NGC 4501	1.3	0.9	$-0.75 \pm 0.10^c$
IC 3476	1.7	1.8	$-0.81 \pm 0.1^a$
NGC 4522	1.0	1.6	$-0.48 \pm 0.10^b$
IC 800	–	2.2	$< -0.76^a$
NGC 4548	–	5.5	$-1.32 \pm 0.10^d$
NGC 4569	2.5	2.0	$-0.55 \pm 0.10^b$
NGC 4607	1.6	1.5	$-0.70 \pm 0.10^d$
NGC 4634	2.0	1.8	$-0.66 \pm 0.10^e$
NGC 4654	3.0	3.0	$-0.87 \pm 0.10^d$

**Notes.** The 1.4 GHz flux densities for the spectral index estimation are taken from: <sup>a</sup> NVSS ( $4\sigma$  upper limits Condon et al. 1998); <sup>b</sup> Murphy et al. (2009), <sup>c</sup> Vollmer et al. (2010); <sup>d</sup> measured from the maps provided by Chung et al. (2009) and <sup>e</sup> Boselli et al. (2015).

## 5. Discussion

### 5.1. Radio-SFR relations

In Fig. 4, our best-fitting radio SFR relations are displayed. As expected, our result for the non-interacting galaxies is in good agreement with Heesen et al. (2022), who worked on galaxies which are nearby and are not members of a cluster. Comparison of our relation for the non-RPS objects with the work of Gürkan et al. (2018) shows that their relation is shifted towards higher radio luminosity, in particular towards the low SFRs. These authors also used LOFAR data, but their sample extends to significantly larger redshifts and has a mean stellar mass that is 2.5 times higher than in our work. We argue that the mass-dependency can mitigate the discrepancy between the various relations, taking into account the mean stellar mass of the samples can account for a discrepancy of  $\approx 0.1$  dex in Fig. 4. Roberts et al. (2021a) on the other hand studied a sample of 95 jellyfish galaxies in low-redshift clusters and found a relation even above our RPS sample. In agreement with the picture that RPS increases the radio-SFR ratio, this relation is closest to the ones for our RPS sample. Indeed, the fact that the relation of Roberts et al. (2021a) is offset to higher radio luminosities compared to our relations for the RPS sample could be explained by the more efficient RPS for the objects in the Roberts et al. (2021a) sample, since they are mostly in clusters that are more massive than Virgo. It was also previously reported that Coma and A1367, more massive nearby clusters, show a greater radio excess compared to Virgo (see Boselli & Gavazzi 2006, and references therein).

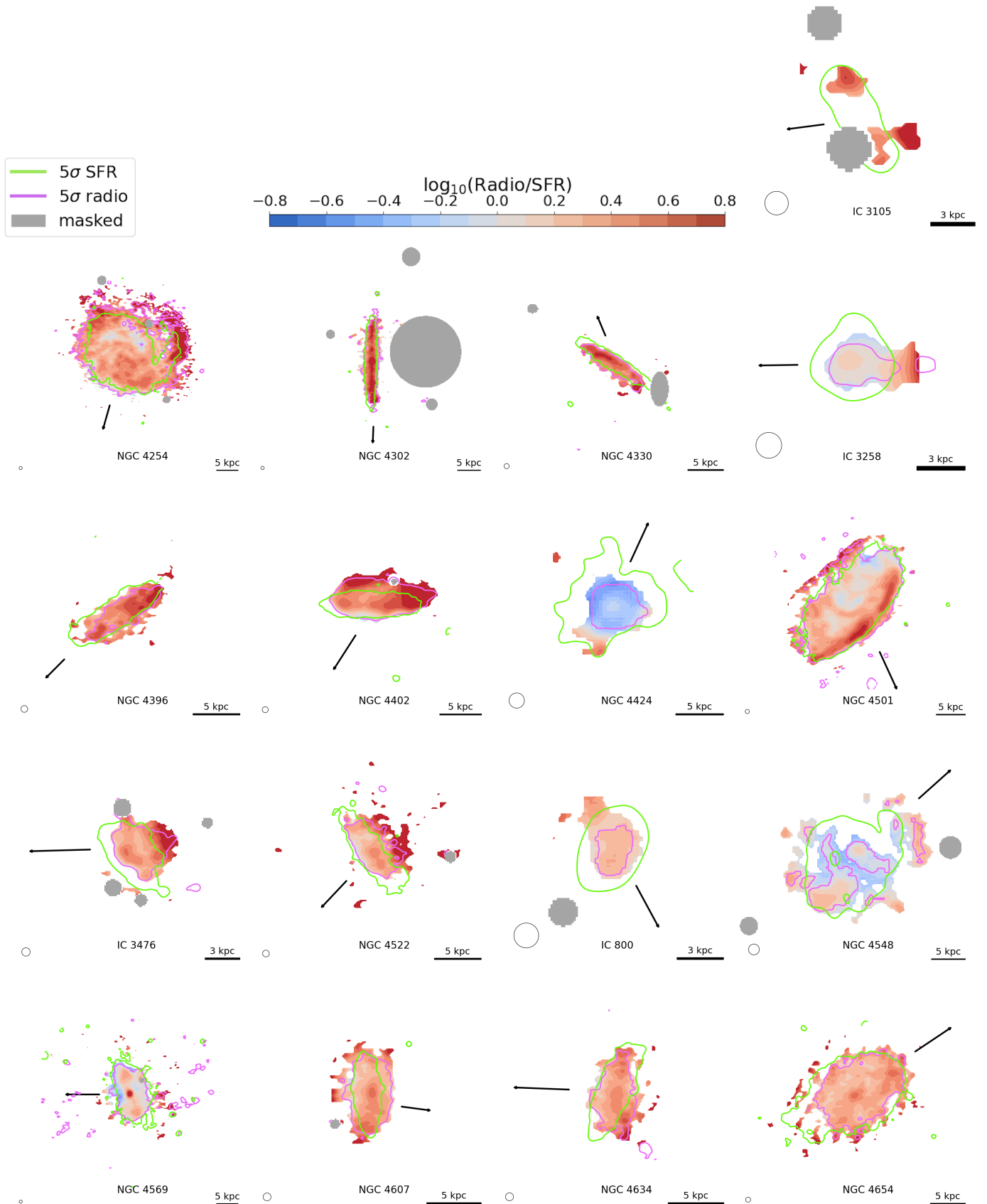


Fig. 8: Logarithmic ratio between the observed and modeled radio emission. The color-scale is symmetric and increases in increments of 0.1 dex, red colors indicate a local radio excess, blue colors a radio deficit and gray areas are masked background sources. Magenta and green lines are the  $5\sigma$  contours of  $B_{\text{obs}}$  and  $\Sigma_{\text{SFR}}$ , respectively. The black arrow indicates the approximate orbit of the galaxy as inferred from the direction of the tail. The circles in the bottom left correspond to the angular resolution of the radio data, which is  $9''$ , except for IC 3105, IC 3258, NGC 4424, IC 800 and NGC 4654 where we used maps at  $20''$  resolution.

That galaxies suffering from RPS do not follow the radio-SFR relation of normal star-forming galaxies but show a higher radio luminosity is well established now due to observations in nearby galaxy clusters. In our RPS sample, this radio excess is widespread ( $\sim 14/17$  objects) and ranges from 0.1 to 0.5 dex (Murphy et al. 2009), in line with previous radio continuum studies of the cluster (e.g. S. Niklas 1995; Murphy et al. 2009).

## 5.2. Spectral index of RPS galaxies

We additionally report for the first time tentative evidence for a spectral index-mass relation for RPS galaxies that is shifted to steeper spectral index values compared to normal star-forming galaxies (Fig. 7). While the significance of this result is currently limited by the availability of uniform, high-fidelity continuum data at 1.4 GHz, it is noteworthy that also other studies reported steep spectral indices for a number of objects suffering from RPS (Chen et al. 2020; Müller et al. 2021; Ignesti et al. 2022b). The spectral steepening is indicative of a CRe population that is of higher radiative age.

Little is known about the spectral indices of RPS galaxies, with studies mostly limited to a few or individual object (Vollmer et al. 2013; Chen et al. 2020; Müller et al. 2021; Ignesti et al. 2022b; Lal et al. 2022; Roberts et al. 2022). A multitude of effects that could explain the enhanced radio luminosity of RPS galaxies are also able to influence the spectral properties of this population. Particle (re-)acceleration due to ISM-ICM shocks could introduce an additional source of CRe (Murphy et al. 2009) with an injection spectral index that may differ from acceleration at supernova shocks associated with star-forming activity. In front of a galaxy moving at a velocity greater than the speed of sound  $c_s$  through the ICM, a bow shock is expected to form (Stevens et al. 1999). In principle, particle acceleration may occur at this bow shock, or at reverse shocks launched into the ISM. The bow shock should be  $\sim 1.5$  kpc in front of the galaxy depending on its size of the galaxy and velocity (Farris & Russell 1994). Due to high speed of sound ( $c_s \sim 500$  km s $^{-1}$ , e.g. Simionescu et al. (2017)) in the ICM, the shock acceleration will take place in the low Mach number regime. That means that the injection spectral index of the shock (Drury 1983):

$$\alpha_{\text{inj}}(\mathcal{M}) = -\frac{\mathcal{M}^2 + 1}{\mathcal{M}^2 - 1} + 0.5 \quad (8)$$

will be steeper than the  $\sim -0.5$  in high Mach-number SN explosions. While a significant contribution of CRe accelerated at the bow shock to the total radio emission of RPS galaxies could thus explain both the radio excess and the steeper spectral indices for this population, we do not consider this scenario since we do not observe radio emission  $\sim 1 - 2$  kpc in advance of the leading edges of the galaxies, the only exceptions are NGC 4607 and NGC 4634. Conversely, these regions are oftentimes deficient in radio emission, as already reported by Murphy et al. (2009). As alternative to the acceleration at the bow-shock, CRe could instead be accelerated at reverse shocks launched into the ISM. However, due to the lower temperature of the ISM and the correspondingly slow speed of sound, these shocks would then again be in the high Mach-number regime resulting in  $\alpha_{\text{inj}} \sim -0.5$ , such that they would not lead to a steepening of the synchrotron spectrum. Thus, we do not consider acceleration due to ISM-ICM shocks as mechanism that can explain steeper radio spectral indices for RPS galaxies.

Another scenario is that of an enhanced magnetic field strength due to compression of the ISM magnetic field (Boselli

& Gavazzi 2006) or the magnetic draping mechanism (Dursi & Pfrommer 2008; Pfrommer & Dursi 2010). This effect would cause a steepening of the synchrotron spectrum, since the loss time  $t_{\text{sync}}$  would decrease compared to the escape time  $t_{\text{esc}}$ , meaning that more spectral aging can occur before the CRe escape the galaxy. In this scenario, the enhancement of the radio emission should also be localized at the leading edge, where the magnetic field compression takes place. This mechanism is supported by the detection of asymmetric polarized ridges in some of the Virgo cluster RPS galaxies (e.g. Vollmer et al. 2008; Pfrommer & Dursi 2010). If the magnetic fields are enhanced due to leading-edge compression of the ISM, the corresponding gas compression could possibly introduce relevant ionization capture losses for low-energy electrons. Those compete with the fast radiative losses at high electron energy due to the accelerated radiative aging in shaping the observed synchrotron spectral index.

As third scenario, Ignesti et al. (2022b) suggested a rapid quenching of the SFR due to the environmental interaction as explanation for the radio excess. This would translate to a strong reduction of SFR $_{\text{H}\alpha}$  after a delay of only few Myr but would only affect  $L_{144}$  at later times due to the lifetime of the massive O-B stars and the cosmic rays that contribute to the 144 MHz synchrotron emission. The availability of UV data presents us with the opportunity to constrain the quenching scenario, since it probes time scales in between the H $\alpha$  and 144 MHz continuum emission (Kennicutt & Evans 2012; Leroy et al. 2012). This scenario would also lead to a steeper radio spectrum for the RPS galaxies due to the declining injection of fresh CRe, resulting in an increased average radiative age of the CRe.

## 5.3. Model scenarios

In the following, we will analyze the phenomenology of simple homogeneous models for the third and second scenario mentioned above. We consider the following version of the momentum-space Fokker-Planck-equation (ignoring diffusion and re-acceleration processes) to describe the evolution of the electron spectrum  $N(E, t)$  as a function of time  $t$  and energy  $E$ :

$$\frac{\partial N(E, t)}{\partial t} = \frac{\partial}{\partial E} [N(E, t)b(E)] - \frac{N(E, t)}{t_{\text{esc}}} + Q(E, t). \quad (9)$$

Here,  $t_{\text{esc}}$  is the CRe escape time for which we employ a value of 50 Myr (see e.g. Dörner et al. 2023) and  $b(E)$  describes the energy losses. In the case of synchrotron and inverse Compton losses,  $b(E) = b_0 E^2$  with:

$$b_0 = 3.2 \times 10^{-6} \left( B^2/2\mu_0 + u_{\text{rad}} \right) \text{ m}^3 \text{ MeV}^{-2} \text{ Myr}^{-1}, \quad (10)$$

where we assume a photon field of energy density  $u_{\text{rad}} = 6 \times 10^5$  eV m $^{-3}$  and synchrotron radiation in a magnetic field  $B = 10$   $\mu$ G (Sarazin 1999). For the source term  $Q(E, t) = qE^{-\delta}$  we consider the injection of electrons with an power-law shock-acceleration spectrum with an exponent of  $\delta = -2$  and a normalization factor  $q$ . The full model and numerical solution of Eq. 9 and the calculation of the radio, FUV and H $\alpha$  emission are described in Appendix C.

We start from the equilibrium state electron spectrum, which corresponds to a spectral index of  $\alpha = -0.77$ . We then consider two scenarios: (1) the RPS causes a quenching of the SFR, modeled by an exponential decay of the source term  $Q(E)$  with an e-folding time scale of  $t_{\text{quench}}$  by a factor  $\exp(-t/t_{\text{quench}})$ ; and (2) compression of the ISM magnetic field enhances the magnetic field of a galaxy by a factor of  $f_B$ .

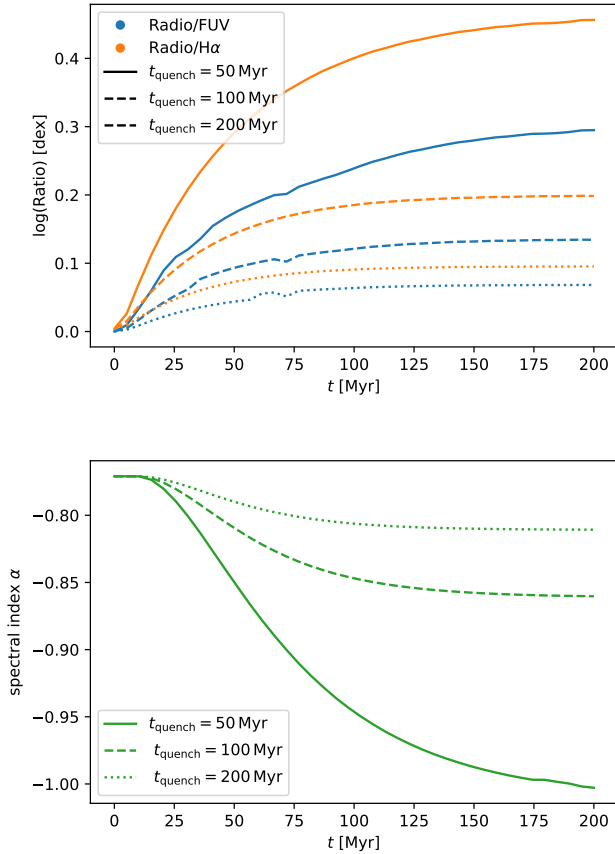


Fig. 9: Scenario (1) – quenched star formation model. *Top panel:* Log-ratio of the 144 MHz to FUV emission (blue) and H $\alpha$  emission (orange) for a quenching time of 50 Myr (solid lines), 100 Myr (dashed lines) and 200 Myr (dotted lines) as a function of time since the onset of SFR-quenching. The ratios are relative to  $t = 0$ . *Bottom panel:* Evolution of the 144 MHz to 1.4 GHz spectral index for the two models.

For scenario (1), the exponential SFR history is of course a simplification valid only for the recent star-forming history ( $\sim$  few 100 Myr). However, this parametrization with only one free parameter allows us to describe the basic effects of a declining SFR due to RPS. In Fig. 9, we show the time evolution of the observed radio-FUV and radio-H $\alpha$  ratio (normalized to 1 at  $t = 0$ ) and the radio spectral index for this scenario with quenching time scales of 50, 100 and 200 Myr. In the model with  $t_{\text{quench}} = 50$  Myr, we can reproduce the observed enhancement of  $\sim 0.4$  dex in the radio-H $\alpha$  ratio and a significant steepening of the radio spectral index of  $\Delta\alpha \approx 0.2$ , in agreement with our tentative evidence of steeper spectral indices for RPS galaxies. Higher values of  $t_{\text{quench}}$  cause a less severe steepening and radio excess. A property of this model is that, due to the longer life time of the stars responsible for the FUV emission, the radio-FUV ratio should be less enhanced compared to the radio-H $\alpha$  ratio. Indeed for three of the objects with the highest radio excesses (NGC 4330, NGC 4501 and NGC 4522) we find that the distance to the best-fitting relation is stronger relative to  $\text{SFR}_{\text{H}\alpha}$  and weaker relative to  $\text{SFR}_{\text{FUV}}$  (see Fig. 6). However, for the remaining objects, no trend can be identified and we also find no significant difference in the  $\text{SFR}_{\text{UV}}/\text{SFR}_{\text{H}\alpha}$  ratios for the RPS and non-RPS sample. For the quenching sce-

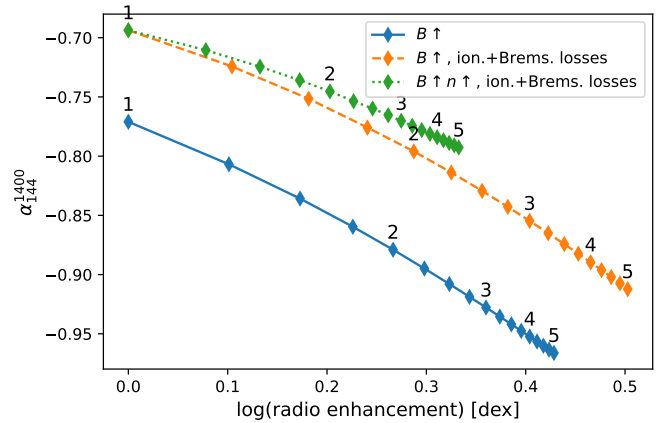


Fig. 10: Scenario (2) – compression model. Effect of an increase of the initial  $10\mu\text{G}$  magnetic field on the radio excess and synchrotron spectrum (blue continuous line). Diamond symbols mark the fractional increase of the magnetic field in increments of 0.25, integer values are highlighted. The orange dashed line shows the same model when including ionization and Bremsstrahlung losses. The green dotted line shows the same model when also increasing the gas density by the same amount as the magnetic field.

nario (1) to fully explain the radio excess and the steep radio spectra of RPS galaxies, violent quenching of the star formation activity with  $t_{\text{quench}} \leq 100$  Myr would need to be a widespread phenomenon and should also imprint in a systematic excess of UV to H $\alpha$  emission, which we only observe for NGC 4330, NGC 4330 and NGC 4522. Spectral energy density fitting of Virgo cluster galaxies yields similarly short quenching time scales for NGC 4330 and NGC 4522 (Boselli et al. 2016). Less violent quenching will still yield some contribution to the radio excess and spectral steepening, but cannot fully explain the observations.

In scenario (2), we model the effect of an increase of the magnetic field strength by a factor of  $f_B$ . This boosts the synchrotron emission and also steepens the spectral index. In the limit  $t_{\text{syn}} \gg t_{\text{esc}}$ , the electron spectrum is escape-dominated and the corresponding radio slope approaches  $\alpha = (\delta - 1)/2 = -0.5$ . In the opposite case of high magnetic field strength ( $t_{\text{esc}} \gg t_{\text{syn}}$ ), it is loss-dominated and the radio slope is close to  $\alpha = \delta/2 = -1$ . For the initial state with  $B = 10\mu\text{G}$ , the spectral index is  $\alpha = -0.77$ . The blue line in Fig. 10 shows the change in radio emission and spectral index for different values of  $f_B$ . An increase of the magnetic field by  $f_B = 1.5$  steepens the spectral index to  $\alpha = -0.84$  and increases the synchrotron emission by 0.17 dex, for  $f_B = 2$ , we find a spectral index of  $\alpha = -0.88$  with a radio enhancement of 0.27 dex. To explain the galaxies with the strongest excesses of  $\geq 0.4$  dex, we would require an increase in the magnetic field strength by  $f_b > 4$  (corresponding to a factor of 16 in energy). The quoted values represent the equilibrium states, but we note that during the ramp-up phase of the magnetic field, the radio emission will be higher and the spectral index may be steeper while the ‘surplus’ electrons (compared to the new equilibrium state) are being depleted. Also, less drastic increases of the magnetic field can be required to explain the enhanced radio emission if the electron distribution is strongly dominated by other processes than synchrotron radiation, i.e. in the case of strong Bremsstrahlung and ionization losses (see e.g. Basu et al. 2015). If we extend our model by ion-

ization and Bremsstrahlung losses with a gas number density of  $N_{\text{gas}} = 10^6 \text{ m}^{-3}$  (orange line in Fig. 10), we still find a significant steepening ( $\alpha = -0.64$  to  $\alpha = -0.73$ ) and increased radio emission (by 0.3 dex) in the case  $f_B = 2$ . The main effect of ionization losses is that for the same magnetic field strength, the observed radio spectrum is flattened towards low frequencies (thus also explaining why the spectral indices in the model without ionization losses are mostly steeper than the observed ones). A much weaker steepening and radio enhancement is predicted by our model if we assume that the gas density  $n_{\text{gas}}$  is compressed by the same factor as the magnetic field due to the strong ionization losses in such a scenario (green dotted line in Fig. 10). To model the relative importance of gas and magnetic field compression and cosmic ray transport, refined simulations are required.

An important open question in scenario (2) is the nature of physical mechanism that is able to increase the magnetic field in RPS galaxies. With simulations, Farber et al. (2022) were able to reproduce a magnetic field enhancement due to compression in the range  $f_B \leq 3$ , however, Tonnesen & Stone (2014) found that increase to only last a short time ( $\sim 25$  Myr). An alternative to the adiabatic compression of the ISM magnetic fields is the magnetic draping mechanism, where the galaxy sweeps up ICM magnetic field lines at the leading edge (Dursi & Pfrommer 2008). It was proposed to explain the asymmetric polarized radio emission for a number of Virgo cluster galaxies (Pfrommer & Dursi 2010). The main difficulty of both mechanisms is that they generate a magnetic field enhancement localized at the leading edge. This is only clearly the case in NGC 4501, where the leading edge radio excess (see Fig. 8 corresponds well with the asymmetric polarized radio emission (e.g. Vollmer et al. 2007; Vollmer et al. 2008). Many other galaxies in the RPS sample (e.g. NGC 4330, NGC 4396, NGC 4402, NGC 4522, IC 3476) even show a deficit of radio continuum emission in that region, likely due to the fast advection of CR or locally efficient ionization losses, amplified by the ISM compression. The compression or magnetic draping scenario can also not easily explain the enhanced radio emission across the disk that is observed for most galaxies. However, the limited angular resolution of our maps, the varying alignment between the galaxy disks and the velocity vector combined with projection effects (the line of sight velocity relative to M 87 is commonly  $\sim 1000$  km/s, indicating significant radial stripping, see Tab. 1) complicate the identification of such local signatures. Tuned simulations may be required to investigate if the observed disk-wide radio enhancement can be generated by magnetic field enhancement and projection effects alone.

## 6. Conclusion

In this paper, we analyzed a sample of 17 Virgo cluster galaxies with a radio morphology indicative of RPS. This sample contains galaxies with masses as low as  $7.8 \times 10^7 M_{\odot}$ . Our LOFAR observations allowed the identification of four new RPS candidates (NGC 4607, NGC 4634, IC 800, IC 3258) and four new objects with radio continuum tails (NGC 4302, NGC 4424, IC 3105, IC 3476) in the cluster. We compare them to a statistical sample of 120 nearby star-forming galaxies in the HRS. Using 144 MHz observations of the LOFAR HBA Virgo Cluster Survey and LoTSS together with the multi-wavelength data of the HRS, our findings are:

- The galaxies in the statistical sample without signs of environmental perturbation in LOFAR follow a super-linear radio-SFR relation with a slope of  $1.39 \pm 0.06$  and  $1.42 \pm 0.06$

compared to H $\alpha$  and FUV-based SFRs, in good agreement with previous low-frequency studies of nearby galaxies.

- Considering the stellar mass as additional parameter in the radio-SFR relation results in fits with comparable scatter ( $\geq 0.25$  dex), supporting a mass-dependent calorimetric efficiency of star-forming galaxies.
- We find a clear radio-excess for the RPS sample, with radio luminosities that are a factor of 2-3 higher compared to the radio-SFR relation for normal star-forming galaxies. Qualitatively, we find the strongest radio excess in galaxies with pronounced radio tails.
- We derived a radio spectral index-total mass relation of the non-RPS galaxies that is in excellent agreement with the literature. For the RPS sample, we find a relation that is shifted towards lower spectral index values by  $\Delta\alpha \approx 0.15$ .
- We model the expected radio emission based on a pure diffusion scenario and hybrid NUV+100  $\mu\text{m}$  SFR surface densities. Comparing the observed to the expected emission, we find that the radio excess is of global nature and mostly extends across the disks. In a number of cases, we can confirm leading-edge radio-deficit regions as a signature of RPS. Only for NGC 4501 we find a leading-edge radio enhancement.
- The radio excess and spectral steepening can be explained by variations in SF history only for NGC 4330, NGC 4396 and NGC 4522 which show the highest radio excesses, which are also accompanied by FUV excesses. This explanation would require rapid quenching with e-folding times  $\leq 100$  Myr.
- Alternatively, an increased magnetic field due to RPS is also able to generate both enhanced radio emission and a steeper synchrotron spectrum. A doubling of the magnetic field strength can explain a moderate enhancement of the radio luminosity ( $\leq 0.27$  dex) and steepening ( $\Delta\alpha \approx 0.1$ ). To explain the highest radio excesses with magnetic field increase only, a strong enhancement of more than a factor of four would be required.

This study allowed us for the first time to test different models for the radio excess, with the emerging picture that there are multiple realistic channels which can contribute to anomalous radio continuum properties of RPS galaxies. In extreme RPS galaxies, a rapid quenching of the star-forming activity may be a relevant mechanism to explain excess radio emission, however, for the broad population of objects suffering from RPS, magnetic field enhancement likely dominates. In the near future, our Virgo Cluster multi-Telescope Observations on Radio of Interacting galaxies and AGN (ViCTORIA) project will allow to further constrain the non-thermal physical mechanisms at play in RPS galaxies with deep, polarized L-band observations by MeerKAT and ultra-low frequency measurements with the LOFAR Low-Band Antenna. Crucially, with the homogeneous multi-frequency data, we will be able to definitely confirm or reject the claim presented in this paper that RPS galaxies in the Virgo cluster show steeper radio spectral indices than normal SF galaxies. Further, we will be able to perform high-fidelity spatially resolved studies of the spectral index and to probe the magnetic field structure using polarization information.

*Acknowledgements.* HE acknowledges support by the Deutsche Forschungsgemeinschaft (DFG, German Research Foundation) under project number 427771150. MB acknowledges funding by the Deutsche Forschungsgemeinschaft under Germany's Excellence Strategy – EXC 2121 “Quantum Universe” – 390833306. FdG acknowledges support from the ERC Consolidator Grant ULU 101086378. AI acknowledges funding from the European Research Council (ERC) under the European Union's Horizon 2020 research and innovation programme (grant agreement No. 833824, PI Poggianti) and the INAF founding program ‘Ricerca Fondamentale 2022’ (PI A. Ignesti). LOFAR (van Haarlem et

al. 2013) is the Low Frequency Array designed and constructed by ASTRON. It has observing, data processing, and data storage facilities in several countries, which are owned by various parties (each with their own funding sources), and that are collectively operated by the ILT foundation under a joint scientific policy. The ILT resources have benefited from the following recent major funding sources: CNRS-INSU, Observatoire de Paris and Université d'Orléans, France; BMBF, MIWF-NRW, MPG, Germany; Science Foundation Ireland (SFI), Department of Business, Enterprise and Innovation (DBEI), Ireland; NWO, The Netherlands; The Science and Technology Facilities Council, UK; Ministry of Science and Higher Education, Poland; The Istituto Nazionale di Astrofisica (INAF), Italy. This research made use of the Dutch national e-infrastructure with support of the SURF Cooperative (e-infra 180169) and the LOFAR e-infra group. The Jülich LOFAR Long Term Archive and the German LOFAR network are both coordinated and operated by the Jülich Supercomputing Centre (JSC), and computing resources on the supercomputer JUWELS at JSC were provided by the Gauss Centre for Supercomputing e.V. (grant CHTB00) through the John von Neumann Institute for Computing (NIC). This research made use of the University of Hertfordshire high-performance computing facility and the LOFAR-UK computing facility located at the University of Hertfordshire and supported by STFC [ST/P000096/1], and of the Italian LOFAR IT computing infrastructure supported and operated by INAF, and by the Physics Department of Turin university (under an agreement with Consorzio Interuniversitario per la Fisica Spaziale) at the C3S Supercomputing Centre, Italy.

## References

- Akritas, M. G. & Bershad, M. A. 1996, *ApJ*, 470, 706
- Astropy Collaboration, Price-Whelan, A. M., Lim, P. L., et al. 2022, *ApJ*, 935, 167
- Baldwin, J. A., Phillips, M. M., & Terlevich, R. 1981, *PASP*, 93, 5
- Basu, A., Beck, R., Schmidt, P., & Roy, S. 2015, *MNRAS*, 449, 3879
- Beck, R. & Krause, M. 2005, *Astronomische Nachrichten*, 326, 414
- Berkhuijsen, E. M., Beck, R., & Tabatabaei, F. S. 2013, *MNRAS*, 435, 1598
- Boselli, A., Boissier, S., Cortese, L., et al. 2006, *ApJ*, 651, 811
- Boselli, A., Cortese, L., & Boquien, M. 2014a, *A&A*, 564, A65
- Boselli, A., Cortese, L., Boquien, M., et al. 2014b, *A&A*, 564, A67
- Boselli, A., Cuillandre, J. C., Fossati, M., et al. 2016, *A&A Suppl. Ser.*, Volume 587, id.A68, 17 pp., 587, A68
- Boselli, A., Eales, S., Cortese, L., et al. 2010, *PASP*, 122, 261
- Boselli, A., Fossati, M., Consolandi, G., et al. 2018, *A&A*, 620, A164
- Boselli, A., Fossati, M., Cuillandre, J. C., et al. 2018a, *A&A*, 615, A114
- Boselli, A., Fossati, M., Ferrarese, L., et al. 2018b, *A&A*, 614, A56
- Boselli, A., Fossati, M., Gavazzi, G., et al. 2015, *A&A*, 579, A102
- Boselli, A., Fossati, M., Roediger, J., et al. 2023a, *A&A*, 669, A73
- Boselli, A., Fossati, M., & Sun, M. 2022, *A&ARev.*, 30, 3
- Boselli, A. & Gavazzi, G. 2006, *PASP*, 118, 517
- Boselli, A., Hughes, T. M., Cortese, L., Gavazzi, G., & Buat, V. 2013, *A&A*, 550, A114
- Boselli, A., Lupi, A., Epinat, B., et al. 2021, *A&A*, 646, 139
- Boselli, A., Roehlly, Y., Fossati, M., et al. 2016, *A&A*, 596, A11
- Boselli, A., Serra, P., de Gasperin, F., et al. 2023b, *A&A*, 676, A92
- Boselli, A., Voyer, E., Boissier, S., et al. 2014, *A&A*, 570, A69
- Bothun, G. D. & Dressler, A. 1986, *ApJ*, 301, 57
- Cantiello, M., Blakeslee, J. P., Ferrarese, L., et al. 2018, *ApJ*, 856, 126
- Catinella, B., Schiminovich, D., Cortese, L., et al. 2013, *MNRAS*, 436, 34
- Chabrier, G. 2003, *PASP*, 115, 763
- Chang, J. & Cooper, G. 1970, *Journal of Computational Physics*, 6, 1
- Chen, H., Sun, M., Yagi, M., et al. 2020, *MNRAS*, 496, 4654
- Chung, A., Van Gorkom, J. H., Kenney, J. D., Crawl, H., & Vollmer, B. 2009, *AJ*, 138, 1741
- Chung, A., van Gorkom, J. H., Kenney, J. D. P., & Vollmer, B. 2007, *ApJ*, 659, L115
- Cid Fernandes, R., Stasińska, G., Mateus, A., & Vale Asari, N. 2011, *MNRAS*, 413, 1687
- Ciesla, L., Boselli, A., Elbaz, D., et al. 2016, *A&A*, 585, A43
- Condon, J. J. 1992, *Ann. Rev. A&A*, 30, 575
- Condon, J. J., Cotton, W. D., Greisen, E. W., et al. 1998, *AJ*, 115, 1693
- Cortese, L., Boissier, S., Boselli, A., et al. 2012, *A&A*, 544, A101
- Cortese, L., Boselli, A., Franzetti, P., et al. 2008, *MNRAS*, 386, 1157
- Cortese, L., Catinella, B., & Smith, R. 2021, *PASA*, 38, e035
- Cortese, L., Fritz, J., Bianchi, S., et al. 2014, *MNRAS*, 440, 942
- Cramer, W. J., Kenney, J. D. P., Cortes, J. R., et al. 2020, *ApJ*, 901, 95
- Crawl, H. H., Kenney, J. D. P., van Gorkom, J. H., & Vollmer, B. 2005, *AJ*, Volume 130, Issue 1, pp. 65-72., 130, 65
- Davies, J. I., Baes, M., Bendo, G. J., et al. 2010, *A&A*, 518, 48
- Dey, A., Schlegel, D. J., Lang, D., et al. 2019, *AJ*, 157, 168
- Dörner, J., Reichherzer, P., Becker Tjus, J., & Heesen, V. 2023, *A&A*, 669, A111
- Drury, L. O. 1983, *Reports on Progress in Physics*, 46, 973
- Dursi, L. J. & Pfrommer, C. 2008, *ApJ*, 677, 993
- Edler, H. W., de Gasperin, F., Brunetti, G., et al. 2022, *A&A*, 666, A3
- Edler, H. W., de Gasperin, F., Shimwell, T. W., et al. 2023, *A&A*, 676, A24
- Engelbracht, C. W., Blaylock, M., Su, K. Y. L., et al. 2007, *PASP*, 119, 994
- Farber, R. J., Ruszkowski, M., Tonnesen, S., & Holguin, F. 2022, *MNRAS*, 512, 5927
- Farris, M. H. & Russell, C. T. 1994, *J. Geophys. Res.*, 99, 17681
- Ferrarese, L., Côté, P., Cuillandre, J.-C., et al. 2012, *ApJS*, 200, 4
- Fossati, M., Mendel, J. T., Boselli, A., et al. 2018, *A&A*, 614, A57
- Gavazzi, G. 1978, *A&A*, 69, 355
- Gavazzi, G. & Boselli, A. 1999, *A&A*, v.343, p.93-99 (1999), 343, 93
- Gavazzi, G., Boselli, A., & Kennicutt, R. 1991, *AJ*, 101, p.1207, 101, 1207
- Gavazzi, G., Boselli, A., Mayer, L., et al. 2001, *ApJ Let.*, 563, L23
- Gavazzi, G., Consolandi, G., Belladitta, S., Boselli, A., & Fossati, M. 2018, *A&A*, 615, A104
- Gavazzi, G., Contursi, A., Carrasco, L., et al. 1995, *A&A*, 304, 325
- Gil de Paz, A., Boissier, S., Madore, B. F., et al. 2007, *ApJ Suppl.*, 173, 185
- Gómez-López, J. A., Amram, P., Epinat, B., et al. 2019, *A&A*, 631, A71
- Gürkan, G., Hardcastle, M. J., Smith, D. J. B., et al. 2018, *MNRAS*, 475, 3010
- Hales, S. E. G., Baldwin, J. E., & Warner, P. J. 1988, *MNRAS*, 234, 919
- Harwood, J. J., Hardcastle, M. J., Croston, J. H., & Goodger, J. L. 2013, *MNRAS*, 435, 3353
- Haynes, M. P., Giovanelli, R., & Kent, B. R. 2007, *ApJ*, 665, L19
- Heckman, T. M. 1980, *A&A*, 87, 152
- Heesen, V., Buie, E., Huff, C. J., et al. 2019, *A&A*, 622, A8
- Heesen, V., de Gasperin, F., Schulz, S., et al. 2023a, *A&A*, 672, A21
- Heesen, V., Klocke, T. L., Brüggem, M., et al. 2023b, *A&A*, 669, A8
- Heesen, V., Staffehl, M., Basu, A., et al. 2022, *A&A*, 664, A83
- Hummel, E. & Saikia, D. J. 1991, *A&A*, 249, 43
- Ignesti, A., Vulcani, B., Botteon, A., et al. 2023, *A&A*, 675, A118
- Ignesti, A., Vulcani, B., Poggianti, B. M., et al. 2022a, *ApJ*, 937, 58
- Ignesti, A., Vulcani, B., Poggianti, B. M., et al. 2022b, *ApJ*, 924, 64
- Kennicutt, R. C., J. 1983, *AJ*, 88, 483
- Kennicutt, Robert C., J. 1998, *ApJ*, 498, 541
- Kennicutt, R. C. & Evans, N. J. 2012, *Ann. Rev. A&A*, 50, 531
- Köppen, J., Jáchym, P., Taylor, R., & Palouš, J. 2018, *MNRAS*, 479, 4367
- Lal, D. V., Lyskova, N., Zhang, C., et al. 2022, *ApJ*, 934, 170
- Lequeux, J., Maucherat-Joubert, M., Deharveng, J. M., & Kunth, D. 1981, *A&A*, 103, 305
- Leroy, A. K., Bigiel, F., de Blok, W. J. G., et al. 2012, *AJ*, 144, 3
- Leroy, A. K., Sandstrom, K. M., Lang, D., et al. 2019, *ApJ Suppl.*, 244, 24
- Longair, M. S. 2010, *High energy astrophysics* (Cambridge university press)
- Madau, P. & Dickinson, M. 2014, *Ann. Rev. A&A*, 52, 415
- Martin, D. C., Fanson, J., Schiminovich, D., et al. 2005, *ApJ Let.*, 619, L1
- Mei, S., Blakeslee, J., Cote, P., et al. 2007, *ApJ*, 655, 144
- Müller, A., Poggianti, B. M., Pfrommer, C., et al. 2021, *Nature Astronomy*, 5, 159
- Murphy, E. J., Condon, J. J., Schinnerer, E., et al. 2011, *ApJ*, 737, 67
- Murphy, E. J., Kenney, J. D., Helou, G., Chung, A., & Howell, J. H. 2009, *ApJ*, 694, 1435
- Nemmen, R. S., Georganopoulos, M., Guiriec, S., et al. 2012, *Science*, 338, 1445
- Pfrommer, C. & Dursi, L. J. 2010, *Nature Physics*, 6, 520
- Poggianti, B. M., Moretti, A., Gullieuszik, M., et al. 2017, *ApJ*, 844, 48
- Roberts, I. D. & Parker, L. C. 2020, *MNRAS*, 495, 554
- Roberts, I. D., Van Weeren, R. J., Mcgee, S. L., et al. 2021a, *A&A*, 650
- Roberts, I. D., van Weeren, R. J., Mcgee, S. L., et al. 2021b, *A&A*, 652, A153
- Roberts, I. D., Van Weeren, R. J., Timmerman, R., et al. 2022, *A&A*, 658, A44
- Roberts, I. D., van Weeren, R. J., Timmerman, R., et al. 2022, *A&A*, 658, A44
- S. Niklas, U. Klein, R. W. 1995, *A&A*, 293, 56
- Sarazin, C. L. 1999, *ApJ*, 520, 529
- Shimwell, T. W., Hardcastle, M. J., Tasse, C., et al. 2022, *A&A*, 659, A1
- Simionescu, A., Werner, N., Mantz, A., Allen, S. W., & Urban, O. 2017, *MNRAS*, 469, 1476
- Stein, Y., Bomans, D. J., Kamphuis, P., et al. 2018, *A&A*, 620, A29
- Stevens, I. R., Acreman, D. M., & Ponman, T. J. 1999, *MNRAS*, 310, 663
- Tasse, C., Shimwell, T., Hardcastle, M. J., et al. 2021, *A&A*, 648, A1
- Tonnesen, S. & Stone, J. 2014, *ApJ*, 795, 148
- van Haarlem, M. P., Wise, M. W., Gunst, A. W., et al. 2013, *A&A*, 556, A2
- Völk, H. J. & Xu, C. 1994, *Infrared Physics and Technology*, 35, 527
- Vollmer, B. 2003, *A&A*, 398, 525
- Vollmer, B., Beck, R., Kenney, J. D. P., & van Gorkom, J. H. 2004, *AJ*, 127, 3375
- Vollmer, B., Braine, J., Combes, F., & Sofue, Y. 2005, *A&A*, 441, 473
- Vollmer, B., Cayatte, V., Boselli, A., Balkowski, C., & Duschl, W. J. 1999, *A&A*, 349, 411
- Vollmer, B., Huchtmeier, W., & Van Driel, W. 2005, *A&A*, 439, 921
- Vollmer, B., Soida, M., Beck, R., et al. 2013, *A&A*, 553, A116
- Vollmer, B., Soida, M., Beck, R., et al. 2007, *A&A Suppl. Ser.*, 464, L37
- Vollmer, B., Soida, M., Braine, J., et al. 2012, *A&A*, 537, A143
- Vollmer, B., Soida, M., Chung, A., et al. 2010, *A&A*, Volume 512, id.A36, 15 pp., 512, A36
- Vollmer, B., Soida, M., Chung, A., et al. 2008, *A&A*, 483, 89
- Vollmer, B., Wong, O. I., Braine, J., Chung, A., & Kenney, J. D. P. 2012, *A&A*, 543, A33
- Vulcani, B., Poggianti, B. M., Gullieuszik, M., et al. 2018, *The Astrophysical Journal Letters*, 866, L25
- Watts, A. B., Cortese, L., Catinella, B., et al. 2023, *PASA*, 40, e017
- Weżgowiec, M., Urbanik, M., Beck, R., Chyży, K. T., & Soida, M. 2012, *A&A*, 545, A69
- Weżgowiec, M., Urbanik, M., Vollmer, B., et al. 2007, *A&A*, 471, 93
- Yagi, M., Yoshida, M., Komiyama, Y., et al. 2010, *AJ*, 140, 1814

## Appendix A: LOFAR data

Table A.1: LOFAR data.

Name	$S_{144}$ [Jy]	$d$ [Mpc]	$L_{144}$ [W Hz <sup>-1</sup> ]	$\alpha_{144}^{1400}$
(1)	(2)	(3)	(4)	(5)
HRS 2	(1.5±0.3)e-2	18.44	(6.1±1.3)e+20	-0.47 ± 0.11 <sup>a</sup>
IC 610	(2.0±0.4)e-2	16.71	(6.5±1.3)e+20	-0.58 ± 0.11 <sup>a</sup>
NGC 3254	(3.4±0.5)e-2	19.37	(1.5±0.2)e+21	< -1.25 <sup>a</sup>
NGC 3277	(1.8±0.3)e-2	20.21	(8.8±1.4)e+20	-0.58 ± 0.09 <sup>a</sup>
HRS 10	(8.2±1.3)e-3	21.66	(4.6±0.8)e+20	-0.56 ± 0.13 <sup>a</sup>
NGC 3287	(2.8±0.6)e-2	18.93	(1.2±0.2)e+21	-0.39 ± 0.10 <sup>a</sup>
HRS 12	(3.4±0.8)e-3	19.89	(1.6±0.4)e+20	< -0.27 <sup>a</sup>
NGC 3294	(2.3±0.3)e-1	22.47	(1.4±0.2)e+22	-0.70 ± 0.08 <sup>a</sup>
NGC 3338	(7.1±1.4)e-2	18.57	(2.9±0.6)e+21	-0.40 ± 0.10 <sup>a</sup>
NGC 3346	(3.0±0.6)e-2	18.0	(1.2±0.2)e+21	-0.34 ± 0.10 <sup>a</sup>
NGC 3380	(1.1±0.2)e-2	22.91	(7.1±1.2)e+20	-0.68 ± 0.12 <sup>a</sup>
NGC 3381	(2.9±0.4)e-2	23.29	(1.9±0.3)e+21	-0.70 ± 0.09 <sup>a</sup>
NGC 3395	(3.9±0.6)e-1	23.1	(2.5±0.4)e+22	-0.64 ± 0.08 <sup>a</sup>
NGC 3424	(3.0±0.4)e-1	21.44	(1.6±0.2)e+22	-0.75 ± 0.08 <sup>a</sup>
NGC 3430	(1.4±0.2)e-1	22.64	(8.7±1.3)e+21	-0.68 ± 0.08 <sup>a</sup>
NGC 3437	(2.6±0.5)e-1	18.24	(1.0±0.2)e+22	-0.59 ± 0.10 <sup>a</sup>
HRS 26	(4.8±0.8)e-3	22.41	(2.9±0.5)e+20	< -0.42 <sup>a</sup>
NGC 3442	(4.6±0.7)e-2	24.77	(3.4±0.5)e+21	-0.56 ± 0.08 <sup>a</sup>
NGC 3451	(3.0±0.6)e-2	19.03	(1.3±0.3)e+21	-0.43 ± 0.10 <sup>a</sup>
NGC 3448	(1.9±0.3)e-1	19.63	(8.6±1.3)e+21	-0.54 ± 0.08 <sup>a</sup>
NGC 3504	(8.8±1.3)e-1	21.94	(5.1±0.8)e+22	-0.51 ± 0.08 <sup>a</sup>
NGC 3512	(3.8±0.6)e-2	19.61	(1.7±0.3)e+21	-0.56 ± 0.08 <sup>a</sup>
NGC 3596	(5.8±1.2)e-2	17.04	(2.0±0.4)e+21	-0.51 ± 0.10 <sup>a</sup>
NGC 3629	(2.1±0.4)e-2	21.53	(1.2±0.2)e+21	-0.46 ± 0.10 <sup>a</sup>
NGC 3631	(4.3±0.6)e-1	16.5	(1.4±0.2)e+22	-0.72 ± 0.08 <sup>a</sup>
NGC 3655	(1.6±0.3)e-1	21.43	(8.6±1.7)e+21	-0.43 ± 0.10 <sup>a</sup>
NGC 3657	(9.1±1.4)e-3	17.2	(3.2±0.5)e+20	-0.39 ± 0.10 <sup>a</sup>
NGC 3666	(5.1±1.0)e-2	15.14	(1.4±0.3)e+21	-0.45 ± 0.10 <sup>a</sup>
NGC 3684	(6.4±1.6)e-2	16.54	(2.1±0.5)e+21	-0.64 ± 0.11 <sup>a</sup>
NGC 3683	(4.9±0.7)e-1	24.4	(3.5±0.5)e+22	-0.69 ± 0.08 <sup>a</sup>
NGC 3686	(8.7±1.8)e-2	16.51	(2.8±0.6)e+21	-0.74 ± 0.10 <sup>a</sup>
NGC 3729	(6.8±1.0)e-2	15.14	(1.9±0.3)e+21	-0.51 ± 0.08 <sup>a</sup>
HRS 61	(4.3±0.7)e-3	17.39	(1.6±0.3)e+20	< -0.37 <sup>a</sup>
NGC 3755	(3.2±0.5)e-2	22.44	(2.0±0.3)e+21	-0.57 ± 0.08 <sup>a</sup>
NGC 3756	(2.8±0.4)e-2	18.41	(1.1±0.2)e+21	-0.81 ± 0.09 <sup>a</sup>
NGC 3795	(3.7±0.6)e-3	17.33	(1.3±0.2)e+20	< -0.31 <sup>a</sup>
NGC 3794	(1.0±0.2)e-2	19.76	(4.8±0.8)e+20	< -0.74 <sup>a</sup>
NGC 3813	(3.4±0.5)e-1	20.97	(1.8±0.3)e+22	-0.57 ± 0.08 <sup>a</sup>
HRS 67	(6.2±1.0)e-3	20.51	(3.1±0.5)e+20	-0.34 ± 0.11 <sup>a</sup>
HRS 68	(1.1±0.2)e-2	20.17	(5.6±0.8)e+20	-0.49 ± 0.10 <sup>a</sup>
NGC 3898	(3.9±0.6)e-2	16.73	(1.3±0.2)e+21	-0.78 ± 0.08 <sup>a</sup>
NGC 3953	(2.4±0.4)e-1	15.0	(6.4±1.0)e+21	-0.75 ± 0.08 <sup>a</sup>
NGC 3982	(2.5±0.4)e-1	15.83	(7.6±1.1)e+21	-0.61 ± 0.08 <sup>a</sup>
HRS 76	(4.7±0.8)e-3	15.27	(1.3±0.2)e+20	-0.18 ± 0.11 <sup>a</sup>
NGC 4100	(2.1±0.3)e-1	15.31	(6.0±0.9)e+21	-0.60 ± 0.08 <sup>a</sup>
NGC 4178	(5.6±1.2)e-2	16.5	(1.8±0.4)e+21	-0.38 ± 0.10 <sup>a</sup>
IC 3061	(1.2±0.3)e-2	16.5	(3.8±0.9)e+20	< -0.80 <sup>a</sup>
NGC 4207	(3.4±0.7)e-2	16.5	(1.1±0.2)e+21	-0.25 ± 0.10 <sup>a</sup>
NGC 4212	(1.3±0.3)e-1	16.5	(4.1±0.8)e+21	-0.72 ± 0.10 <sup>a</sup>
NGC 4216	(6.4±1.3)e-2	16.5	(2.1±0.4)e+21	-0.72 ± 0.10 <sup>b</sup>
NGC 4222	(1.3±0.3)e-2	16.5	(4.4±1.0)e+20	-0.58 ± 0.12 <sup>a</sup>
NGC 4237	(2.3±0.5)e-2	16.5	(7.5±1.7)e+20	-0.58 ± 0.11 <sup>a</sup>
IC 3105 <sup>†</sup>	(4.0±1.1)e-3	16.5	(1.3±0.4)e+20	< -0.36 <sup>c</sup>
NGC 4254 <sup>†</sup>	(2.5±0.5)e+0	16.5	(8.3±1.7)e+22	-0.77 ± 0.10 <sup>a</sup>
NGC 4289	(1.5±0.4)e-2	16.5	(4.8±1.2)e+20	-0.53 ± 0.12 <sup>b</sup>



Table A.1: continued.

Name	$S_{144}$ [Jy]	$d$ [Mpc]	$L_{144}$ [W Hz <sup>-1</sup> ]	$\alpha_{144}^{1400}$
(1)	(2)	(3)	(4)	(5)
NGC 4294	(8.6±1.7)e-2	16.5	(2.8±0.6)e+21	-0.51 ± 0.10 <sup>b</sup>
NGC 4298	(1.3±0.3)e-1	16.5	(4.2±0.8)e+21	-0.88 ± 0.10 <sup>d</sup>
NGC 4302 <sup>†</sup>	(2.5±0.5)e-1	16.5	(8.0±1.6)e+21	-0.77 ± 0.10 <sup>a</sup>
NGC 4303	(2.0±0.4)e+0	16.5	(6.5±1.3)e+22	-0.67 ± 0.10 <sup>a</sup>
NGC 4307	(9.5±2.1)e-3	23.0	(6.0±1.4)e+20	-0.57 ± 0.14 <sup>a</sup>
NGC 4312	(3.6±0.7)e-2	16.5	(1.2±0.2)e+21	-0.50 ± 0.10 <sup>a</sup>
NGC 4316	(2.1±0.4)e-2	23.0	(1.3±0.3)e+21	-0.54 ± 0.10 <sup>c</sup>
NGC 4321	(1.5±0.3)e+0	16.5	(4.9±1.0)e+22	-0.74 ± 0.10 <sup>d</sup>
NGC 4330 <sup>†</sup>	(5.6±1.1)e-2	16.5	(1.8±0.4)e+21	-0.63 ± 0.11 <sup>a</sup>
NGC 4343	(4.2±0.9)e-2	23.0	(2.7±0.5)e+21	-1.01 ± 0.11 <sup>b</sup>
IC 3258 <sup>†</sup>	(9.8±2.1)e-3	16.5	(3.2±0.7)e+20	< -0.74 <sup>a</sup>
NGC 4351	(2.0±0.4)e-2	16.5	(6.5±1.3)e+20	< -1.03 <sup>a</sup>
IC 3268	(8.0±1.9)e-3	23.0	(5.1±1.2)e+20	-0.26 ± 0.12 <sup>a</sup>
NGC 4359	(1.1±0.2)e-2	17.9	(4.2±0.7)e+20	< -0.77 <sup>a</sup>
NGC 4370	(1.1±0.2)e-2	23.0	(6.8±1.5)e+20	< -0.77 <sup>a</sup>
NGC 4376	(5.0±1.4)e-3	23.0	(3.1±0.9)e+20	< -0.43 <sup>b</sup>
NGC 4380	(2.0±0.4)e-2	23.0	(1.2±0.3)e+21	< -0.68 <sup>a</sup>
NGC 4383	(1.2±0.2)e-1	16.5	(3.9±0.8)e+21	-0.45 ± 0.10 <sup>a</sup>
VCC 827	(5.1±1.1)e-2	23.0	(3.2±0.7)e+21	-0.59 ± 0.10 <sup>a</sup>
NGC 4390	(1.8±0.4)e-2	23.0	(1.1±0.2)e+21	< -0.98 <sup>d</sup>
IC 3322	(1.9±0.4)e-2	23.0	(1.2±0.3)e+21	-0.79 ± 0.12 <sup>d</sup>
NGC 4396 <sup>†</sup>	(9.6±1.9)e-2	16.5	(3.1±0.6)e+21	-0.79 ± 0.10 <sup>a</sup>
NGC 4402 <sup>†</sup>	(4.3±0.9)e-1	16.5	(1.4±0.3)e+22	-0.81 ± 0.10 <sup>a</sup>
NGC 4413	(8.8±1.9)e-3	16.5	(2.9±0.6)e+20	< -0.68 <sup>a</sup>
NGC 4412	(4.0±0.9)e-2	16.5	(1.3±0.3)e+21	-0.44 ± 0.11 <sup>d</sup>
NGC 4416	(1.8±0.4)e-2	16.5	(6.0±1.3)e+20	-0.57 ± 0.11 <sup>a</sup>
NGC 4424 <sup>†</sup>	(3.0±0.6)e-2	23.0	(1.9±0.4)e+21	-0.67 ± 0.11 <sup>a</sup>
NGC 4430	(2.5±0.5)e-2	23.0	(1.6±0.3)e+21	-0.57 ± 0.10 <sup>b</sup>
VCC 1091	(6.1±1.4)e-3	23.0	(3.9±0.9)e+20	-0.25 ± 0.12 <sup>a</sup>
NGC 4450	(4.3±0.9)e-2	16.5	(1.4±0.3)e+21	-0.71 ± 0.10 <sup>a</sup>
NGC 4451	(2.1±0.4)e-2	23.0	(1.3±0.3)e+21	-0.52 ± 0.10 <sup>b</sup>
IC 3392	(8.2±1.8)e-3	16.5	(2.7±0.6)e+20	-0.44 ± 0.13 <sup>a</sup>
NGC 4457	(8.0±1.7)e-2	16.5	(2.6±0.5)e+21	-0.45 ± 0.10 <sup>a</sup>
NGC 4470	(2.1±0.4)e-2	16.5	(7.0±1.4)e+20	-0.14 ± 0.10 <sup>a</sup>
NGC 4480	(2.2±0.5)e-2	16.5	(7.1±1.6)e+20	-0.86 ± 0.13 <sup>a</sup>
NGC 4491	(7.5±2.0)e-3	16.5	(2.4±0.7)e+20	< -0.61 <sup>a</sup>
NGC 4505	(2.7±0.6)e-2	16.5	(8.7±2.0)e+20	< -1.15 <sup>d</sup>
IC 797	(1.1±0.2)e-2	16.5	(3.6±0.8)e+20	< -0.78 <sup>a</sup>
NGC 4501 <sup>†</sup>	(1.8±0.4)e+0	16.5	(6.0±1.2)e+22	-0.75 ± 0.10 <sup>a</sup>
IC 3476 <sup>†</sup>	(5.0±1.0)e-2	16.5	(1.6±0.3)e+21	-0.81 ± 0.10 <sup>c</sup>
NGC 4519	(6.4±1.3)e-2	16.5	(2.1±0.4)e+21	-0.83 ± 0.10 <sup>a</sup>
NGC 4522 <sup>†</sup>	(8.1±1.6)e-2	16.5	(2.6±0.5)e+21	-0.48 ± 0.10 <sup>a</sup>
NGC 4525	(2.1±0.4)e-3	16.77	(7.2±1.4)e+19	< -0.07 <sup>d</sup>
IC 800 <sup>†</sup>	(1.1±0.2)e-2	16.5	(3.5±0.8)e+20	< -0.76 <sup>b</sup>
NGC 4532	(5.0±1.0)e-1	16.5	(1.6±0.3)e+22	-0.63 ± 0.10 <sup>a</sup>
NGC 4535	(6.4±1.3)e-1	16.5	(2.1±0.4)e+22	-0.96 ± 0.10 <sup>a</sup>
IC 3521	(2.6±0.5)e-2	16.5	(8.3±1.7)e+20	-0.84 ± 0.12 <sup>b</sup>
NGC 4540	(1.4±0.3)e-2	16.5	(4.5±1.0)e+20	-0.64 ± 0.12 <sup>a</sup>
NGC 4548 <sup>†</sup>	(1.1±0.2)e-1	16.5	(3.7±0.8)e+21	-1.32 ± 0.10 <sup>b</sup>
NGC 4565	(8.6±1.7)e-1	17.61	(3.2±0.6)e+22	-0.80 ± 0.10 <sup>b</sup>
NGC 4567	(7.1±1.4)e-2	16.5	(2.3±0.5)e+21	-0.76 ± 0.10 <sup>c</sup>
NGC 4568	(5.8±1.2)e-1	16.5	(1.9±0.4)e+22	-0.60 ± 0.10 <sup>c</sup>
NGC 4569 <sup>†</sup>	(5.5±1.1)e-1	16.5	(1.8±0.4)e+22	-0.55 ± 0.10 <sup>c</sup>
NGC 4579	(6.5±1.3)e-1	16.5	(2.1±0.4)e+22	-0.59 ± 0.10 <sup>a</sup>
NGC 4580	(1.2±0.3)e-2	16.5	(3.8±0.9)e+20	< -0.79 <sup>b</sup>
NGC 4595	(9.6±2.2)e-3	16.5	(3.1±0.7)e+20	-0.31 ± 0.12 <sup>b</sup>
NGC 4606	(8.9±2.1)e-3	16.5	(2.9±0.7)e+20	< -0.68 <sup>a</sup>

Table A.1: continued.

Name	$S_{144}$ [Jy]	$d$ [Mpc]	$L_{144}$ [W Hz <sup>-1</sup> ]	$\alpha_{144}^{1400}$
(1)	(2)	(3)	(4)	(5)
NGC 4607 <sup>†</sup>	(9.8±2.0)e-2	16.5	(3.2±0.6)e+21	-0.70 ± 0.10 <sup>a</sup>
NGC 4630	(2.4±0.5)e-2	16.5	(7.9±1.7)e+20	-0.28 ± 0.10 <sup>a</sup>
NGC 4634 <sup>†</sup>	(1.5±0.3)e-1	16.5	(5.0±1.0)e+21	-0.66 ± 0.10 <sup>a</sup>
NGC 4639	(3.7±0.8)e-2	16.5	(1.2±0.3)e+21	-0.68 ± 0.10 <sup>b</sup>
NGC 4647	(3.0±0.6)e-1	16.5	(9.8±2.0)e+21	-0.92 ± 0.10 <sup>a</sup>
NGC 4654 <sup>†</sup>	(8.5±1.7)e-1	16.5	(2.8±0.6)e+22	-0.87 ± 0.10 <sup>a</sup>
NGC 4689	(1.4±0.3)e-1	16.5	(4.6±0.9)e+21	-1.15 ± 0.10 <sup>a</sup>
NGC 4725	(1.8±0.3)e-1	17.27	(6.4±1.0)e+21	-0.79 ± 0.08 <sup>a</sup>
NGC 4747	(1.6±0.3)e-2	16.84	(5.4±0.9)e+20	-0.33 ± 0.08 <sup>a</sup>
NGC 4746	(1.8±0.4)e-1	16.5	(5.9±1.2)e+21	-0.52 ± 0.10 <sup>a</sup>
NGC 4758	(6.7±1.5)e-3	16.5	(2.2±0.5)e+20	-0.34 ± 0.13 <sup>a</sup>
NGC 4779	(2.6±0.5)e-2	16.5	(8.4±1.8)e+20	-0.49 ± 0.10 <sup>a</sup>
NGC 5014	(3.2±0.5)e-2	16.23	(10.0±1.5)e+20	-0.44 ± 0.08 <sup>a</sup>
NGC 5145	(1.3±0.2)e-1	17.5	(4.7±0.7)e+21	-0.58 ± 0.08 <sup>a</sup>
IC 902	(2.1±0.3)e-2	22.97	(1.3±0.2)e+21	-0.46 ± 0.08 <sup>a</sup>
NGC 5248	(5.4±1.1)e-1	16.46	(1.8±0.4)e+22	-0.58 ± 0.10 <sup>a</sup>
NGC 5301	(7.2±1.1)e-2	21.54	(4.0±0.6)e+21	-0.63 ± 0.08 <sup>a</sup>
NGC 5303	(7.4±1.1)e-2	20.27	(3.6±0.5)e+21	-0.46 ± 0.08 <sup>a</sup>
HRS 300	(3.0±0.6)e-3	19.34	(1.4±0.3)e+20	< -0.22 <sup>a</sup>
NGC 5372	(5.2±0.8)e-2	24.53	(3.7±0.6)e+21	-0.51 ± 0.08 <sup>a</sup>
NGC 5486	(9.5±1.5)e-3	19.76	(4.4±0.7)e+20	< -0.71 <sup>a</sup>
HRS 315	(3.2±0.7)e-3	20.57	(1.6±0.4)e+20	< -0.24 <sup>a</sup>
NGC 5645	(4.1±0.9)e-2	19.57	(1.9±0.4)e+21	-0.44 ± 0.10 <sup>a</sup>
NGC 5669	(2.6±0.5)e-2	19.54	(1.2±0.2)e+21	-0.38 ± 0.10 <sup>a</sup>
NGC 5692	(3.0±0.6)e-2	22.59	(1.8±0.4)e+21	-0.68 ± 0.10 <sup>a</sup>

**Notes.** Column (1) lists the galaxy names, objects that are marked with a dagger symbol are in the RPS sample. Column (2) shows the LOFAR flux density measured at 20'' resolution, column (3) the distance (taken from [Boselli et al. \(2010\)](#) for objects outside the Virgo cluster, otherwise assumed to be 16.5 Mpc), column (4) the 144 MHz luminosity and column (5) the spectral index between 144 MHz and 1.4 GHz. The 1.4 GHz flux densities (or upper limits) are taken from <sup>a</sup> [Boselli et al. \(2015\)](#); <sup>b</sup> measured from the maps of [Chung et al. \(2009\)](#); <sup>c</sup> [Murphy et al. \(2009\)](#) and <sup>d</sup> [Vollmer et al. \(2010\)](#).

Appendix B: Radio-SFR maps

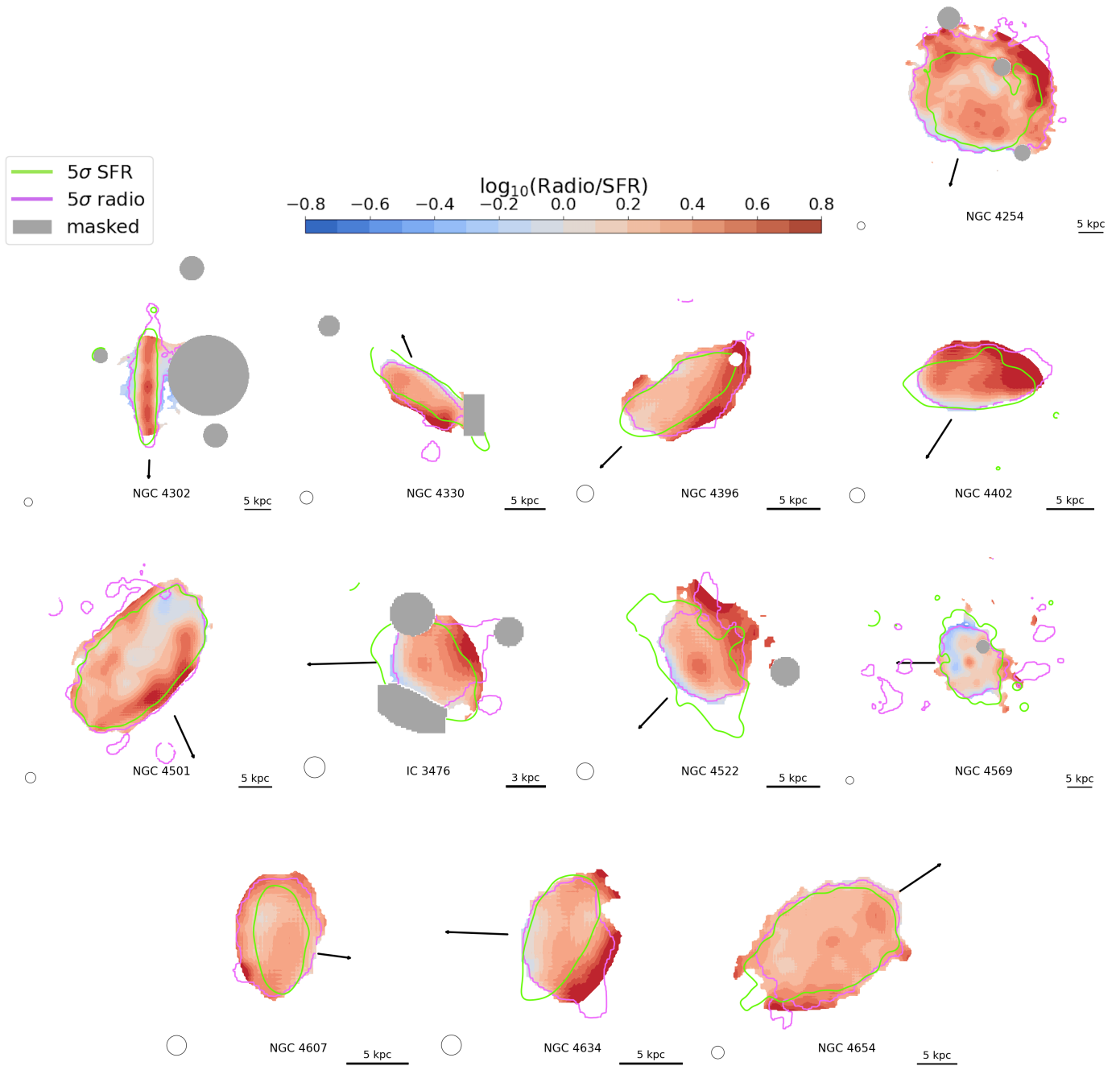


Fig. B.1: Logarithmic ratio between the observed and modeled radio emission. The figure is identical to Fig. 8, except that we only show the images based on the  $20''$  radio maps which were not displayed previously.

## Appendix C: Synchrotron emission model

To numerically solve Eq. 9, we use the Chang-Cooper discretization scheme (Chang & Cooper 1970) implemented in the `pychangcooper`<sup>3</sup> library. We extend this code to include an escape term  $N(E, t)/t_{\text{esc}}$ , a time-dependent injection term  $Q(E, t) = qE^{-2} \exp(-t/t_{\text{quench}})$  and the relevant loss processes, i.e. Synchrotron radiation, inverse Compton scattering, ionization and Bremsstrahlung. Those are described by (Longair 2010):

$$b(E) = b_0 E^2 + N_{\text{gas}} \left( b_1 \left( 3 \log \frac{E}{m_e c^2} + 19.8 \right) + b_2 E \right), \quad (\text{C.1})$$

with  $b_0 = 3.2 \times 10^{-6} (B^2/2\mu_0 + u_{\text{rad}}) \text{ m}^3 \text{ MeV}^{-2} \text{ Myr}^{-1}$ ,  $b_1 = 2.4 \times 10^{-7} \text{ MeV m}^3 \text{ Myr}^{-1}$ , and  $b_2 = 1.2 \times 10^{-8} \text{ m}^3 \text{ Myr}^{-1}$ . Here,  $m_e$  is the electron rest mass,  $c$  the speed of light and  $N_{\text{gas}}$  the gas density. For the latter, we assume that only the H I content contributes and approximate a typical mean density  $N_{\text{gas}} = 4.4 \times 10^5 \text{ m}^{-3}$  assuming the H I mass of NGC 4396  $M_{\text{HI}} = 8.6 \times 10^8 M_{\odot}$  (Chung et al. 2009) is distributed in a cylinder with a radius of 5 kpc and a height of 1 kpc.

We split the energy domain into 100 logarithmically spaced points ranging from 1 MeV to 100 GeV. The time domain is discretized in steps of 0.1 Myr. For the initial electron spectrum, we use the source term  $Q(E)$  for constant injection and let the spectrum evolve for  $t \gg t_{\text{esc}}$  until it reaches a steady state. This spectrum is then either subject to a time-dependent decrease of the source term on a scale  $t_{\text{quench}}$  or to an increase of the magnetic field by a factor of  $f_B$  and evolved in time.

The flux density of the corresponding synchrotron emission at a frequency  $\nu$  and after a time  $t$  is given by (Harwood et al. 2013):

$$S(\nu, B, t) = S_0 B \int_0^{\pi} d\delta \sin(\delta)^2 \int dE F(x) N(E, B, t), \quad (\text{C.2})$$

where  $\delta$  is the pitch angle,  $S_0$  a normalization constant and  $F(x)$  the following integral of the Bessel function of order 5/3:

$$F(x) = x \int_x^{\infty} K_{5/3}(z) dz. \quad (\text{C.3})$$

The variable  $x = \nu/\nu_c$  is the ratio of the frequency  $\nu$  and the critical frequency  $\nu_c$ , which is given by:

$$\nu_c = \frac{3E^2 e B \sin(\delta)}{4\pi m_e^3 c^4}. \quad (\text{C.4})$$

Here,  $e$  is the electron charge.

For the electron spectrum and the corresponding synchrotron emission, we include a 10 Myr delay between the star formation and the CRe injection due to the lifetime of the massive O and B stars. The FUV and H $\alpha$  emission will also be delayed compared to the star formation, although less severely. We define  $I_{\text{burst}}(t)$  as the time-dependent intensity after an instantaneous burst of star formation, where we use the distribution provided in Leroy et al. (2012). To take into account the contribution of the prior SFR history to the intensity  $I(t)$ , we use the convolution:

$$I(t) = \int \text{SFR}(\tau) I_{\text{burst}}(t - \tau) d\tau. \quad (\text{C.5})$$

In the scenario of reducing SFR due to RPS, the SFR is given by:

$$\text{SFR}(t) = \begin{cases} \text{SFR}_0, & \text{if } t \leq 0 \\ \text{SFR}_0 e^{-\frac{t}{t_{\text{quench}}}}, & \text{otherwise.} \end{cases} \quad (\text{C.6})$$

<sup>3</sup> <https://github.com/grburgess/pychangcooper>